ANNUAL REVIEWS

Annual Review of Materials Research

High-Energy X-Ray Diffraction Microscopy in Materials Science

Joel V. Bernier,[1] Robert M. Suter,[2] Anthony D. Rollett,[2] and Jonathan D. Almer[3]

[1]Lawrence Livermore National Laboratory, Livermore, California 94550, USA; email: bernier2@llnl.gov

[2]Department of Physics and Department of Materials Science and Engineering, Carnegie Mellon University, Pittsburgh, Pennsylvania 15213, USA; email: suter@andrew.cmu.edu, rollett@andrew.cmu.edu

[3]Advanced Photon Source, Argonne National Laboratory, Lemont, Illinois 60439, USA; email: almer@aps.anl.gov

Annu. Rev. Mater. Res. 2020. 50:395–436

The *Annual Review of Materials Research* is online at matsci.annualreviews.org

https://doi.org/10.1146/annurev-matsci-070616-124125

Keywords

high-energy diffraction microscopy, 3DXRD, microstructure, synchrotron, nondestructive measurement, X-rays, 3D characterization

Abstract

High-energy diffraction microscopy (HEDM) is an implementation of three-dimensional X-ray diffraction microscopy. HEDM yields maps of internal crystal orientation fields, strain states, grain shapes and locations as well as intragranular orientation distributions, and grain boundary character. Because it is nondestructive in hard materials, notably metals and ceramics, HEDM has been used to study responses of these materials to external fields including high temperature and mechanical loading. Currently available sources and detectors lead to a spatial resolution of ∼1 μm and an orientation resolution of <0.1°. With the penetration characteristic of high energies ($E \geq 50$ keV), sample cross-section dimensions of ∼1 mm can be studied in materials containing elements across much of the Periodic Table. This review describes hardware and software associated with HEDM as well as examples of applications. These applications include studies of grain growth, recrystallization, texture development, orientation gradients, deformation twinning, annealing twinning, plastic deformation, and additive manufacturing. We also describe relationships to other X-ray-based methods as well as prospects for further development.

1. INTRODUCTION

The ability to quantify and visualize materials' microstructure in three dimensions is a recent advance in the long history of microscopy (1). In this review, we focus on X-ray microscopy modalities that use crystal unit cell orientations as the contrast mechanism and use spatially resolved diffraction to achieve such contrast. Many other optical and electron-based microscopies exist and are described in widely available textbooks. Automation of serial sectioning (2) combined with electron backscatter diffraction (EBSD) (3, 4) provides the capability to characterize polycrystalline materials in three dimensions at a resolution of approximately 0.5° and 0.1 μm. This approach is self-evidently destructive, and the limited penetrating power of electrons means that characterization is limited to the surface in experiments that subject the material to deformation or any other change. Moreover, the typical need to repolish the surface means that repeated scanning is not performed on the original surface. By contrast, the far greater penetrating power of high-energy X-rays enables nondestructive three-dimensional (3D) characterization, allowing one to impose as many steps of microstructural evolution as available measurement time allows. The microstructure and crytallographic state in a given volume of material can be followed as they evolve under applied processing. Such data provide unique mesoscopic verification and validation tests for models of material behavior.

The term high-energy diffraction microscopy (HEDM) refers to a suite of synchrotron-based X-ray techniques developed at the Advanced Photon Source (APS) 1-ID beamline at Argonne National Laboratory; similar implementations exist at other high-energy synchrotrons around the world [e.g., the European Synchrotron Radiation Facility (ESRF) in Grenoble, France; the Cornell High Energy Synchrotron Source (CHESS) at Cornell University in Ithaca, New York; Petra-III in Hamburg, Germany; and SPring-8 in Japan], and the techniques are generically called three-dimensional X-ray diffraction microscopy (3DXRD) (5–7). These techniques map crystal lattice orientations and elastic strain states in three dimensions inside bulk polycrystalline materials and can track changes as samples undergo deformation, thermal treatments, or other applied fields. High-energy micro–computed tomography (HE-μCT) is another technique that is frequently combined with HEDM measurements to probe density variations within the measured volumes. Further variants have also been developed. All of these techniques use one and the same sample stage, so it is straightforward to combine the measurements as well as the extracted information so as to construct multiparameter 3D data sets.

As described in recent reviews (8, 9), these methods use a monochromatic X-ray beam of chosen energy (≥50 keV) appropriate for transmission through a particular sample. The sample is rotated about an axis nominally perpendicular to the incident beam, typically over a range $\Delta\omega = 180°$ or 360°. During rotation, one or more high-pixel-count, two-dimensional (2D) area detectors collect successive images of forward-diffracted or transmitted X-rays, integrated over small rotation intervals of width $\delta\omega$. The small diffraction angles associated with high X-ray energies enable the capture of large regions of reciprocal space with area detectors of practical dimensions, leading to overdetermined and robust characterizations.

The three relevant data collection modes are summarized below. Section 2 presents relevant aspects of high-energy X-rays and their diffraction and the basic principles behind the measurement techniques. More detailed aspects of implementation and data processing are described in Section 3, and example applications of HEDM are described in Section 4. Section 5 discusses expected future developments and relationships to other techniques. Future prospects are described in Section 6.

Far-field high-energy diffraction microscopy (ff-HEDM) uses one or more large-format industrial imaging detectors (each of which is typically a 2,048 × 2,048 array with a 200-μm

pixel pitch or a roughly 40 × 40 cm^2 field of view) placed 1 to 1.5 m downstream of the sample. Detector images are integrated over rotation intervals $\delta\omega \geq 0.05^\circ$ over $180^\circ \leq \Delta\omega \leq 360^\circ$. Here, diffraction peaks from individual grains fall approximately on Debye–Scherrer rings, which facilitates a straightforward correlation with sets of Miller indices. A box beam—typically defined by slits—illuminates a 3D volume of the sample. Data collection is usually much faster than in the case of near-field measurements for several reasons: (*a*) The box beam probes an entire volume in a single rotation scan, (*b*) the far-field detector has higher quantum efficiency (for reasons discussed below), and (*c*) the large pixels integrate scattering from a large sample volume (comparable to or larger than grain volume) rather than spatially resolving diffraction spot shapes. Reconstruction identifies subsets of measured Bragg peaks that are consistent with a known crystal structure and orientation. The components of their associated reciprocal lattice vectors form the basis for an optimization problem to determine lattice orientations, center-of-mass positions, and grain- or cross-section-averaged strain tensor values for each grain. Section 2.3 provides a detailed discussion of the procedure, and Section 4 illustrates example applications.

Near-field high-energy diffraction microscopy (nf-HEDM) is a crystal unit cell orientation mapping technique with ~1 μm spatial and 0.1° orientation resolution, and as such is capable of resolving features such as grain boundaries. nf-HEDM uses a high-resolution imaging detector [currently a 2,048 × 2,048 charge-coupled device (CCD) pixel array with a 1.48-μm effective pixel pitch or a roughly 3 × 3 mm^2 field of view] placed 5 to 15 mm downstream of the sample combined with a line-focused incident beam that illuminates a planar cross section. Typically, diffraction images are collected over rotation intervals $0.05 \leq \delta\omega \leq 1^\circ$ over a range of $\Delta\omega = 180^\circ$. Diffraction spot positions on the detector are determined by a combination of their position of origin (i.e., grain position within the sample) and the diffraction geometry. A voxel-by-voxel forward modeling method reconstruction procedure converts the set of diffraction images into an orientation map in a sequence of layers (10, 11). **Figure 1*a*** depicts an example. The nf-HEDM technique has

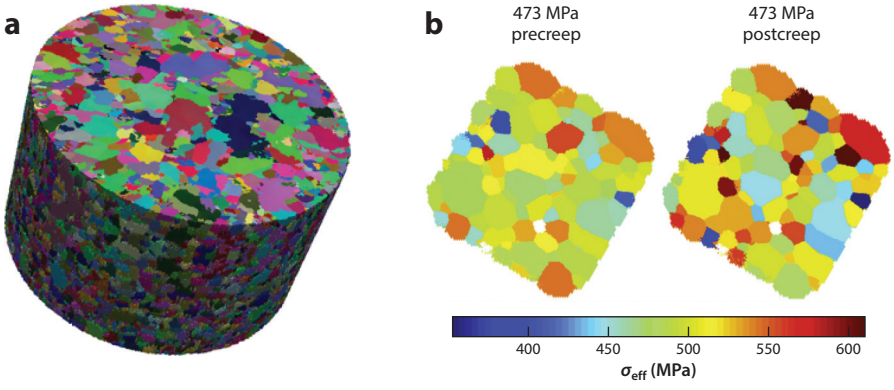

Figure 1

(*a*) Three-dimensional copper microstructure measured with near-field high-energy diffraction microscopy (17). The sample diameter is 1 mm, and the measured volume is 0.4 mm^3. Each reconstructed triangular volume element (voxel) is colored by mapping three orientation parameters to an RGB color scale so that regions of uniform color correspond to crystalline grains. (*b*) A two-dimensional slice of microstructure of a Ti-7Al sample under tensile loading. Near-field-determined grain cross sections are shown, but colors are according to far-field-determined von Mises stress values in each grain cross section. Loading was in the direction perpendicular to the figure. Note the heterogeneous strain states due to significant intergrain interactions. Two states of the sample are shown, one before (*left*) and one after (*right*) 0.6% plastic creep. Figure adapted with permission from Reference 18.

been applied to, for example, elemental metals, ceramics, and application-relevant industrial alloys. Materials have been studied in pristine annealed states (with almost perfect single-crystal grains), as well as in deformed states after tensile (12), cyclic (13), and shock deformation (14). Materials spanning most of the Periodic Table, from aluminum (15) to uranium oxide (16), have been studied. Section 4 describes example applications.

HE-μCT is a high-energy version of conventional tomography. HE-μCT fills in gaps left by the other HEDM measurements: micrometer-resolution determination of sample shape, locations of voids, and maps of secondary phases. Both absorption and phase-contrast information can be collected; the latter yields high sensitivity to boundaries between regions with distinct indices of refraction (e.g., different densities). Tomographic resolution is set largely by the detector's spatial resolution, so the nf-HEDM detector can be used for HE-μCT as well. Alternatively, one can use an even higher resolution detector with 1-μm effective pixels since the needed field of view is set by sample and beam sizes, which are typically less than 2 mm. This data collection procedure is entirely consistent with the HEDM apparatus. For lack of space, we omit additional details of this technique, but we describe its combined use with HEDM in Section 4.

2. HOW HIGH-ENERGY DIFFRACTION MICROSCOPY WORKS

This section presents fundamental aspects and principles of the techniques while avoiding reference to specific implementations to the extent possible. Section 3 describes apparatus and data treatment pipelines associated with the nf-HEDM and ff-HEDM techniques as implemented at the APS 1-ID-E end station. Common to all of these techniques is data acquisition using area detectors, with high-energy monochromatic X-rays being detected in transmission. Samples are rotated to excite many Bragg diffraction peaks, and the detectors sense all intense peaks up to as high an order as the detector geometry allows. Reconstruction of such data requires that the orientations of all illuminated grains (crystals) be determined together, and confidence in (or reliability of) the result is based on how well all the individual diffraction peaks are matched.

2.1. High-Energy X-Rays

HEDM and HE-μCT measurements are performed through measurement of X-rays transmitted through samples and use area detectors of limited size for detection. Both of these requirements motivate the use of high-energy X-rays.

2.1.1. X-ray properties. As demonstrated in **Figure 2**, X-rays with $E \geq 50$ keV penetrate distances of $\gtrsim$1 mm in elemental solids up to $Z = 56$ (barium) and $\gtrsim$100 μm for all materials. In contrast, standard laboratory sources with energies of 8.05 keV (copper K_α) or 17.5 keV (molybdenum K_α) have penetration distances shorter by an order of magnitude or two. Second, high-energy X-rays compress reciprocal space into the forward direction, allowing transmission geometry area detectors to cover large volumes of that space and to detect many Bragg peaks from elemental or larger unit cell materials, as discussed below. HEDM's micrometer-scale resolution in millimeter-sized sample cross sections yields $\sim 10^6$ resolution volumes in illuminated planes, leading to excellent sampling statistics. Volumes of order 1 mm^3 contain $\sim 10^9$ resolution volumes.

An additional convenience of using high-energy X-rays is that absorption lengths in air are measured in meters. That is, evacuated flight paths are not necessary, and diffraction images can be collected either near or several meters downstream of the sample. Furthermore, long focal-length optics and large sample chambers can be used. HEDM measurements take full advantage of all of these features.

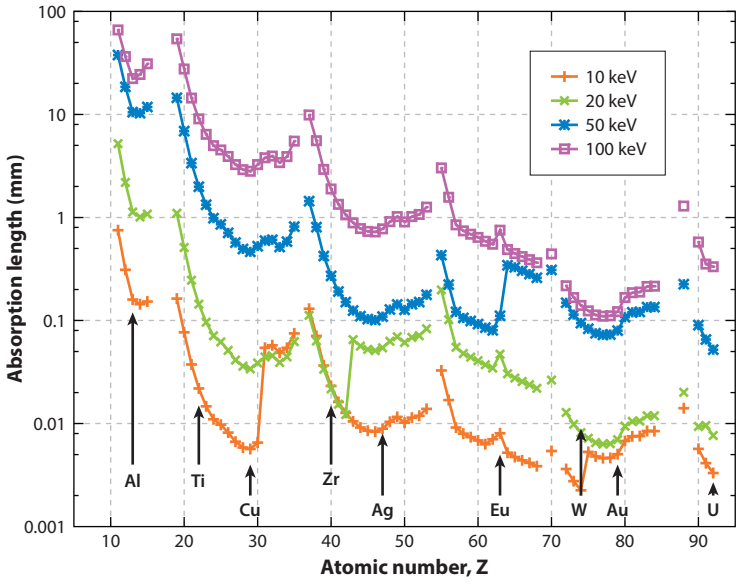

Figure 2

Absorption lengths (1/*e* distances) in elemental solids spanning the Periodic Table for four different photon energies in the hard X-ray regime. The structure of the observed trends is influenced by atomic absorption edges (steps up in penetration with increasing Z) and by variations in material density (peaks at noble gas atomic solids) as one crosses the Table. With 50–100-keV X-rays, one can perform transmission measurements with millimeter-dimension sample cross sections in materials across much of the Table. Figure based on attenuation factors from National Institute of Standards and Technology Standard Reference Database 66 and densities from Reference 19.

Not coincidentally, development of the HEDM techniques began shortly after high-energy synchrotron facilities dedicated to photon sciences were commissioned in the 1990s. Synchrotrons with stored electron energies ≥6 GeV produce copious photon fluxes in the high-energy regime. The 1-ID beamline at APS is now fed by a high-field superconducting undulator that produces world-leading fluxes in this range. While we provide a brief overview in Section 3.1, our focus here is on measurement techniques rather than beamline components and optics. Descriptions of how beams are generated and tailored can be found elsewhere (e.g., 20–24).

2.1.2. Diffraction at high energies. To a large extent, HEDM is based on simple Bragg diffraction from single crystals. In its most elementary form, this is written as

$$n\lambda = 2d \sin\theta, \qquad 1.$$

where λ is the X-ray wavelength; d is the spacing between a set of crystallographic planes; θ, the Bragg angle, is the angle of incidence relative to the planes; and n, a positive integer, is a harmonic number that specifies the number of wavelengths of phase shift that occurs between X-rays scattered from successive planes. Only when Equation 1 is satisfied does constructive interference occur between X-rays scattered from all successive crystallographic planes so as to generate an intense scattered wave. The constructive interference condition for laterally displaced waves within the planes is that the scattering be specular with respect to the lattice planes, which implies that the scattering angle is 2θ and that the normal to the lattice planes bisects the angle between the incident and scattered waves.

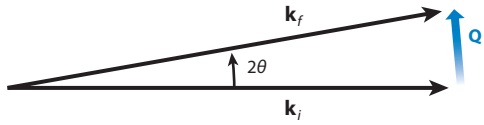

Figure 3

A scattering triangle showing reciprocal space vectors. At high energies, the magnitude, $2\pi/\lambda$, of wavevectors $\mathbf{k}_i$ (incident) and $\mathbf{k}_f$ (scattered) are large compared with the low-order reciprocal lattice vectors, $\mathbf{G}_{hkl}$, associated with Bragg diffraction from crystals; therefore, the Bragg angles, θ, and the scattering angles, 2θ, are small, since $Q = 2k\sin\theta$ and Bragg conditions correspond to $\mathbf{Q} = \mathbf{k}_f - \mathbf{k}_i = \mathbf{G}_{hkl}$.

Below, we use the language of reciprocal space, which is the natural space in which scattering experiments are cast and the Fourier space of the scattering entity (19, 20). A general scattering vector, $\mathbf{Q}$, is defined as

$$\mathbf{Q} = \mathbf{k}_f - \mathbf{k}_i, \qquad 2.$$

where $\mathbf{k}_f$ and $\mathbf{k}_i$ are wavevectors associated with the scattered and incident waves, respectively. For the elastic scattering relevant here, the wavenumber is $|\mathbf{k}_f| = |\mathbf{k}_i| = k = 2\pi/\lambda$. The terms in Equation 2 have reciprocal length units. **Figure 3** depicts a standard scattering triangle appropriate for high energies.

Scattering through wavevector $\mathbf{Q}$ measures modulations in the density of scatterers, that is, the electron density, with wavelength $2\pi/|\mathbf{Q}|$ in the direction of $\mathbf{Q}$. More precisely, the intensity is the squared modulus of the 3D Fourier transform of the density; the 3D transform amounts to a one-dimensional (1D) Fourier transform of the laterally averaged density of scatterers. The averaging over planes perpendicular to $\mathbf{Q}$ yields a function, $\bar{\rho}(r_\parallel)$, where $r_\parallel$ is a position coordinate parallel to $\mathbf{Q}$. In a crystal, $\bar{\rho}(r_\parallel)$ is constant (at the average electron density) unless $r_\parallel$ runs perpendicular to a set of lattice planes; such planes are specified by a set of Miller indices, h, k, and l. Thus, modulations occur only when $\mathbf{Q}$ satisfies this condition, in which case $\bar{\rho}$ is periodic with the period of the plane spacing and the Fourier transform (hence, the measured intensity) contains peaks corresponding to the fundamental spatial frequency and its harmonics. These peaks are the Bragg peaks, and the Bragg condition can be restated as $\mathbf{Q} = \mathbf{G}_{hkl}$. The amplitude of the modulation determines the measured intensity. A perfect crystal at zero temperature contains modulations corresponding to the finite size of constituent atoms. At elevated temperature, vibrations due to finite thermal phonon occupancy smooth the $\bar{\rho}$ functions, reducing the relative intensities of harmonics. Note that only vibrations or displacements along $\mathbf{Q}$ have an effect on the shape of $\bar{\rho}(r_\parallel)$ or the observed intensity. In highly defected or deformed crystals, a similar but nonthermal set of displacements is generated, which again results in reduced intensities on higher-order Bragg peaks. The use of high-energy X-rays allows measurement out to high $|\mathbf{Q}|$ and hence high harmonic number or large h, k, and l values, but, depending on the state of the microstructure, Bragg peaks in this limit may be quite weak. Furthermore, lattice displacements, either thermal or defect generated, give rise to broad, diffuse scattering, which can be seen as an increased background that makes it difficult to extract weak Bragg peaks.

A third way to write the Bragg condition is obtained by setting $\mathbf{Q} = \mathbf{G}_{hkl}$ in Equation 2, squaring and reducing to unit vectors:

$$\hat{\mathbf{G}}_{hkl} \cdot \hat{\mathbf{k}}_i = -\sin\theta_{hkl}. \qquad 3.$$

This form emphasizes that as a sample rotates in an incident beam (see Section 2.2), any (hkl) Bragg peak will be generated whenever the projection of the associated reciprocal lattice vector (RLV) onto the incident beam direction satisfies this equation. Placing an area detector downstream of

the sample allows observation of each such event out to some maximum scattering angle or $|\mathbf{Q}|$ (which, for a noncircular detector, depends on the scattering direction). As long as the RLV is tilted away from the rotation axis by an angle $\chi > \theta_{bkl}$, this condition will be satisfied twice, with $\mathbf{G}_{bkl}$ on either side of the incident beam. Since Bragg angles are small at high energies, a large volume of reciprocal space is available under HEDM experimental conditions. The peaks corresponding to $\mathbf{G}_{bkl}$ and $-\mathbf{G}_{bkl}$ are known as Friedel pairs and are of particular interest in ff-HEDM analysis.

Both HEDM techniques benefit from maximizing the number of diffracted beams recorded from each crystallite/grain in the illuminated volume of material. Each grain yields $\mathcal{O}(100)$ observations in a typical measurement. While these data are highly redundant for the determination of unit cell orientations, the fidelity of grain center-of-mass position and strain state (ff-HEDM) and grain shape (nf-HEDM) improve as both the number and the angular distribution of recorded Bragg reflections increase (see Section 3 for examples).

2.2. The Rotating Crystal Method

HEDM utilizes instrument configurations that are analogous to the standard rotating crystal method (25), which is still widely applied in macromolecular crystallography as well as HE-μCT. The objective is to maximize the number of diffracted beams recorded from each crystallite/grain in the sample. Both the X-ray wavelength and the range of scattering angles subtended by the detectors affect resolution. The Ewald construction illustrates how the reciprocal lattice must be rotated relative to the sphere to activate the different Bragg conditions inside the limiting sphere.

The sample is mounted on a rotation axis, as illustrated by **Figure 4**, that is nominally perpendicular to the incident beam propagation direction (though there are cases where it may be

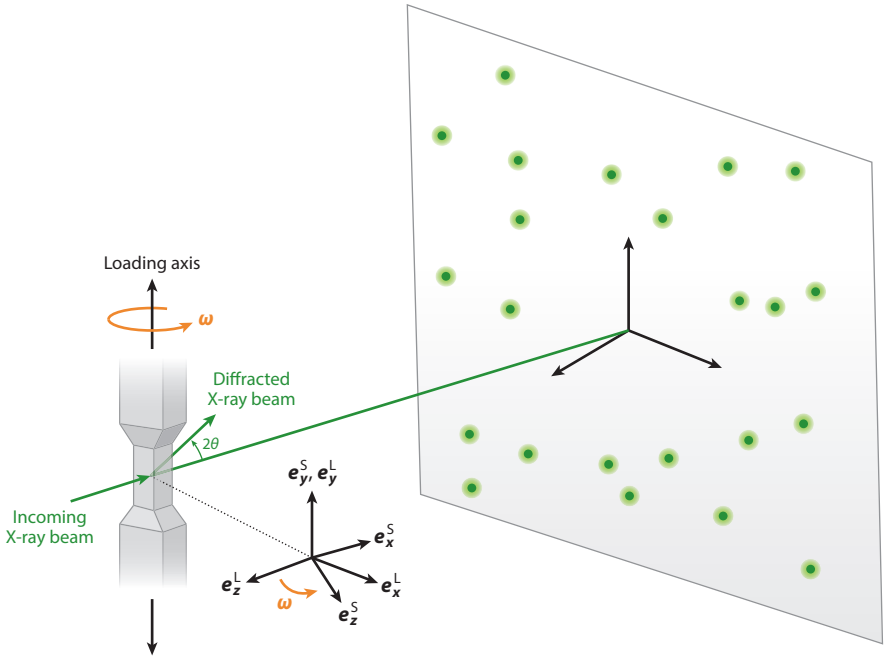

Figure 4

Schematic of the far-field high-energy diffraction microscopy setup, with a specimen subject to uniaxial loading.

advantageous to cant the stage slightly, e.g., radial diffraction in high-pressure experiments using diamond anvil cells). Each detector integrates the incident intensity over a small angular interval, $\delta\omega \leq 1^\circ$, with smaller $\delta\omega$ providing higher resolution at the cost of increased collection time (considering limits in detector readout speed). The total angular range for the measurement of a single volume is ideally $180^\circ \leq \Delta\omega < 360^\circ$ in order to maximize the number of Bragg conditions satisfied. In the nominal configuration, a range of 180° is sufficient to activate all possible reflections twice: the Friedel pair $\mathbf{G}_{bkl}$ and $\mathbf{G}_{\bar{b}\bar{k}\bar{l}}$. Note that in the absence of resonant scattering, Friedel pairs are indistinguishable in that their intensities are equal even if the underlying crystal lattice is not centrosymmetric. Each reflection and its Friedel pair are recorded twice for a range of 360°, yielding four independent measurements associated with the same lattice plane normal. This aspect has implications for systematic error reduction, described further in Section 3.2.4.

The resultant image series collected on each detector form a 3D diffractogram (analogous to a sinogram in tomography), with two axes representing the spatial extent of the detector and the third representing the rotation interval, $\delta\omega$. The intensity, I, of each Bragg reflection comprises a fourth dimension associated with each (i, j, ω) location in the diffractogram: (i, j, ω, I), where (i, j) are Cartesian pixel coordinates, which may be represented equivalently as physical coordinates in the detector plane, $(\mathbf{X}_d, \mathbf{Y}_d)$. **Figure 5** illustrates the simulated diffractogram for a single, centered hexagonal close-packed (HCP) crystal. Each Bragg peak has a distinct intensity distribution around the nominal location that depends on a convolution of instrumental and material factors. These include the energy bandwidth and divergence of the X-ray beam, the gradients of intragranular orientation and strain in the crystal, the volume of the grain, and the distance of the $\mathbf{G}_{bkl}$ from the rotation axis. HEDM data essentially consist of a superposition of such diffractograms from each grain (or resolved subvolume), modulated in $(\mathbf{X}_d, \mathbf{Y}_d)$ by its precession

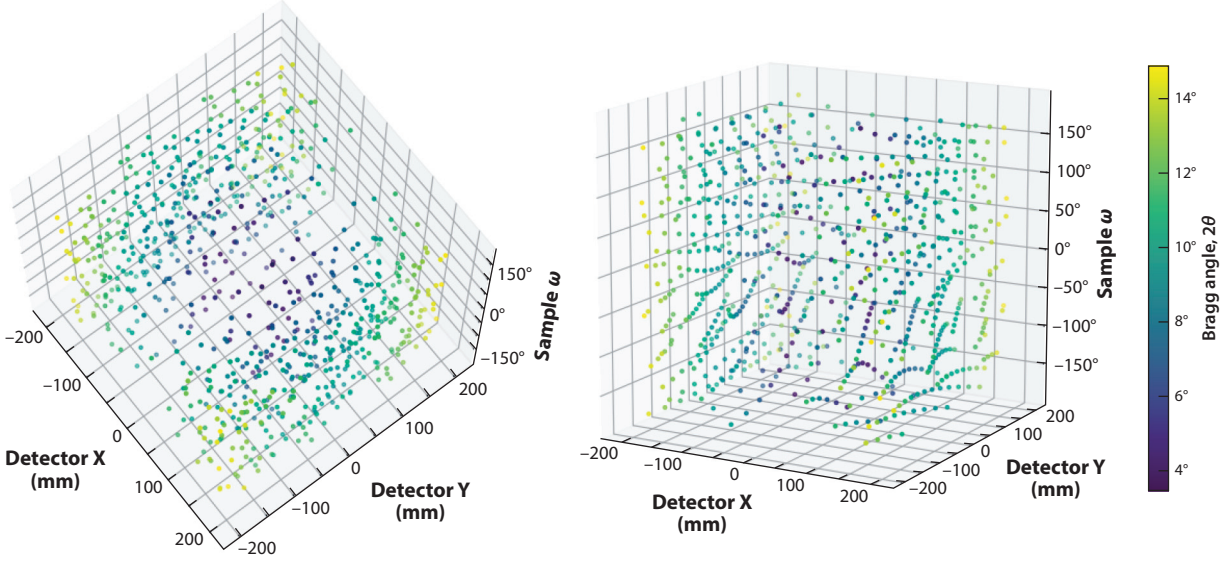

Figure 5

Views of a simulated diffractogram for a single, centered hexagonal close-packed (*P6*/mmc) grain in a symmetric far-field high-energy diffraction microscopy configuration (i.e., the X-ray beam intersects the detector center at normal incidence) with $Q_{\max} \sim 1.83$ Å^{-1}. Each glyph represents a measured Bragg reflection, and its color represents the corresponding Bragg angle, 2θ. Note that the glyphs represent only the locations of the Bragg peaks, not the scattered intensities. The detector face is a 204.8-mm square, which truncates the spots in the $\mathbf{X}_d$–$\mathbf{Y}_d$ plane. The rotation range is a full 360°, yielding 836 total reflections (209 unique $\mathbf{G}_{bkl}$).

about the rotation axis (see Sections 2.3 and 2.4 for more details). The salient differences that distinguish HEDM from the standard rotating crystal method are the use of (*a*) high-energy X-rays for penetration power (e.g., metallic specimens); (*b*) large–field of view X-ray beams [typically $\mathcal{O}(1.5\ \text{mm}^2)$]; (*c*) polycrystalline [up to $\mathcal{O}(10^3)$ grains] rather than single-crystal samples; and (*d*) the high-resolution imaging used in the nf-HEDM variant. The subsequent sections expand on the effects of these points.

2.3. Far-Field High-Energy Diffraction Microscopy

In the far-field configuration, the working distance to each detector is large compared with the illuminated dimensions of the sample (typically $\gtrsim$100 times larger); the divergence of diffracted beams from the path of the incident beam is, in turn, much larger than the sample size. Conversely, the divergence of the diffracted beams emanating from each crystal from the reference Debye–Scherrer rings[1] on the detectors is relatively small. This geometric filtering of the diffracted signals—and the resultant sparsity in the diffractograms—is the most salient feature distinguishing ff-HEDM data from nf-HEDM data. Essentially all of the data reduction implementations discussed in Section 3 exploit this feature.

Beyond the penetration power mentioned in Section 2.1, the use of higher-energy X-rays has the effect of demagnifying reciprocal space and compressing the Bragg angles (see Equation 1). This effect, in conjunction with the large working distance, requires large-format flat-panel detectors to collect data at sufficiently high reciprocal space resolution (typically with $Q_{\text{max}} \sim 2$–$5\ \text{Å}^{-1}$). Detectors from medical imaging systems typically have both the large format and high quantum efficiency at high X-ray energies (26, 27). At APS 1-ID-E, there is an option to use either a single GE 41RT detector or an array of four (usually at twice the working distance) for increased strain sensitivity. Newer detector and instrument designs are increasingly relying on a composite approach to achieve a large detector area while maintaining a relatively small pixel size. The combination of the high brilliance of synchrotron sources and the efficiency and framing speed of currently available detectors ($\gtrsim$10 per second) enables ff-HEDM to be used as an in situ characterization technique (28, 29). The data for an in situ ff-HEDM experiment are effectively four dimensional: a time series of rotation image series measured for each sample state. Typical collection times for a single diffraction volume are on the order of ~0.5–5 min, depending on required exposure time and $\delta\omega$ resolution (see Section 3 for a more detailed discussion of implementation details). As mentioned in Poulsen's (30) excellent review of 3DXRD, the canonical ff-HEDM technique yields intergranular information for each phase in the sample. The first-order quantities accessible in the data are the grain-averaged (*a*) orientation, (*b*) centroidal position, and (*c*) (elastic) distortion. Higher-order quantities such as grain volume and characteristics of orientation and strain distributions are available through more detailed analysis of the intensity distributions comprising each Bragg reflection (e.g., 31–35). We focus primarily on the first-order quantities herein, particularly since more detailed grain morphologies and intragranular orientation distributions are available via nf-HEDM (see Section 2.4).

The primary differentiator between different grains/domains in ff-HEDM is orientation. The crystal orientation determines the gross position of the Bragg reflections in the diffractogram, while the precession and strain manifest as slight modulations of their precise locations. **Figure 6** demonstrates the relative effects of grain precession and strain on Bragg peak locations using simulated diffractograms. Consideration of the digitization and blurring effects of the detector (e.g.,

[1]In other words, the powder pattern that would emanate from an ideal polycrystalline sample of the same crystal structure centered on the rotation axis.

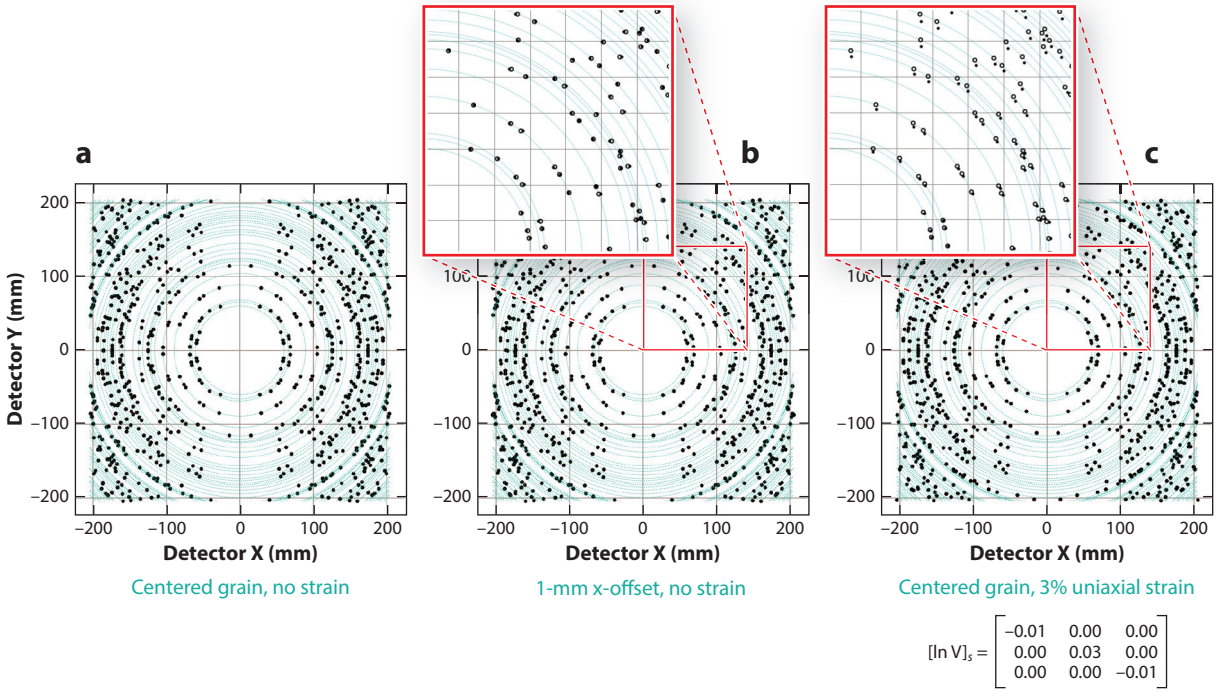

Figure 6

(*a*) An ω-projected view of the simulated diffraction shown in **Figure 5** for a single, centered hexagonal close-packed (*P6*/mmc) grain. The reference Debye–Scherrer rings are plotted in cyan; note that the reflections all fall on these rings for this case. (*b*,*c*) Analogous projections for the same grain with the addition of crystal displacement from (*b*) the rotation axis and (*c*) strain. (*Insets*) The open circles are the reference positions from the centered, unstrained case (see panel *a*). Note that for the displaced case the magnitude of the deviations from the reference positions is independent of 2θ, while for strain the relative effect is larger for increasing 2θ. Also, in the strained case the direction of the deviations reverses from the **X** axis to the **Y** axis in response to the strain varying from (Poisson) contraction to extension. Note that the strain tensor components are depicted as the logarithm of the underlying stretch tensor in the sample frame.

pixel size, point spread) and the X-ray source (e.g., divergence, energy bandwidth) with respect to the relatively small effects of precession and strain reveals a fundamental limitation of ff-HEDM: the inability to distinguish the Bragg reflections from grains having very similar orientations. The exact minimum misorientation limit depends on many factors—including those listed above, with the addition of intragranular orientation spread—but is typically on the order of ~0.5°; that is, the Bragg reflections for separated grains will overlap irrecoverably if their mutual misorientations are below this threshold. The only practical remedy is to place the detector much closer to the sample, which increases the influence precession has on the location of Bragg reflections on the detector. This is the basis for nf-HEDM (see Section 2.4).

The fundamental objective of ff-HEDM analysis is essentially the same as for macromolecular crystallography: indexing and extraction of the individual Bragg reflections emanating from single crystals in the diffractogram. In the former step, each diffraction spot is assigned to a $\mathbf{G}_{hkl}$ consistent with a crystal lattice and unique orientation in the sample frame. In the latter step, information is extracted from each indexed Bragg reflection (e.g., integrated intensity, shape, precise position) as input to additional calculation, which for ff-HEDM encompasses the refinement of the parameters encoding the mean grain orientation (three), centroidal position (three), and strain

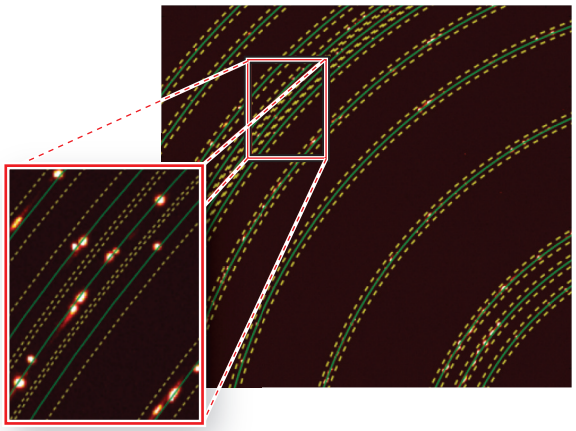

Figure 7

View of a single far-field high-energy diffraction microscopy image for $\delta\omega = 1^\circ$ for a titanium specimen. The green rings denote the reference (strain-free) Debye–Scherrer rings, and the dashed yellow rings denote a range in Bragg angle, 2θ, of $\pm 0.125^\circ$ about them. The ring at bottom right is the lowest-order Bragg reflection, here $\{10\bar{1}0\}$ occurring at $2\theta = 2.57^\circ$. Note that the image is very sparsely populated; the various diffraction spots originate from different grains; the diffraction spots do not lie exactly on the reference Debye–Scherrer rings, reflecting the fact that the grain centroids are displaced from the rotation axis and are possibly distorted (elastically strained); and individual Bragg reflections may be unambiguously associated with a Debye–Scherrer ring even for the moderate-order reflections shown in the inset (the sixth through tenth Debye–Scherrer rings, here from 8.74° to 9.93°).

(six) via optimization or sampling. In contrast to nf-HEDM the indexing and extraction (or refinement) processes can be decoupled in ff-HEDM. The algorithmic details of the indexing and extraction analyses are presented in Section 3.2, while general aspects concerning the character of ff-HEDM data are presented here.

2.3.1. Geometric considerations. As discussed above, ff-HEDM data exhibit geometric filtering: The type of $\mathbf{G}_{hkl}$ for each measured Bragg peak is generally known from the coarse 2θ positions on the detector, with the exception of degeneracy and $\mathbf{G}_{hkl}$ with very similar magnitude (i.e., interplanar spacing). Aside from those cases, the lowest-order reflections are generally well enough separated for most Laue groups to be unambiguously associated with a single Debye–Scherrer ring (hence the symmetrized $\{hkl\}$ family). The spatial filtering of the Bragg reflections is illustrated in **Figure 7**, which shows a selected 1° ω projection from a diffractogram for a titanium specimen. This feature encourages the use of a reference angular coordinate system ($2\theta_{\text{ref}}$, η_{ref}, ω) in lieu of the measured diffractogram coordinates (i, j, ω) or equivalently ($\mathbf{X}_d, \mathbf{Y}_d, \omega$) in the initial indexing of ff-HEDM data, which affords considerable computational expedience. The origin of this reference angular coordinate system is on the rotation axis, which fixes the measurement of (reference) Bragg angle, $2\theta_{\text{ref}}$; and η_{ref} represents the azimuthal coordinate around the Debye–Scherrer rings. Using this coordinate transform, each detector pixel $(i, j) \rightarrow (\mathbf{X}_d, \mathbf{Y}_d)$ corresponds to a unique ($2\theta_{\text{ref}}$, η_{ref}) pair. **Figure 8*a*** shows a typical polycrystalline diffractogram with the reference coordinate system overlaid. Working in the reference angular coordinates removes the need to compute the intersection a specified diffracted ray with the detector plane ($\mathbf{X}_d, \mathbf{Y}_d$) at

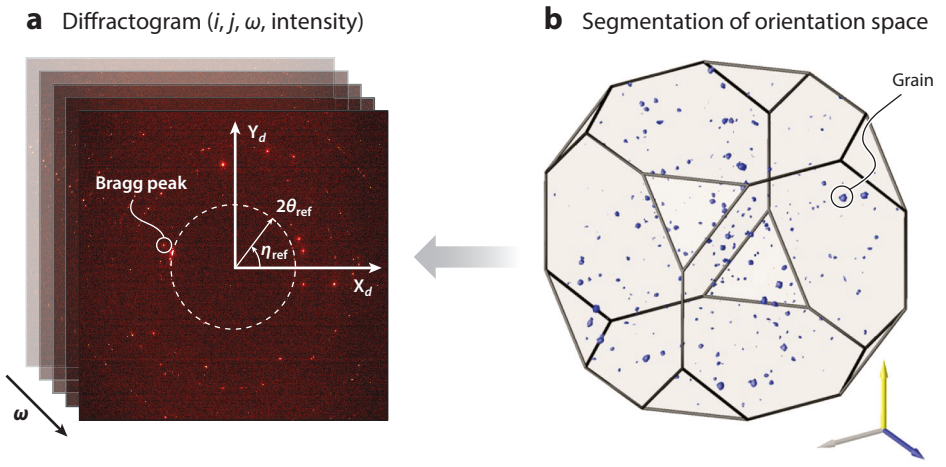

Figure 8

(*a*) Schematic of diffractogram showing Bragg peak signals and definition of the reference angular coordinate system. (*b*) The fundamental region of orientation space for cubic ($m\bar{3}m$) symmetry segmented by the indexing process. The isosurface shown in blue corresponds to a completeness value of 75%; the ratio of predicted diffracted intensities for orientations within these compact clusters is consistent with measured intensities in the diffractogram is >75%. Generally speaking, the average orientations of these clusters correspond to the average orientations of the distinct grains in the diffraction volume probed.

a specified sample orientation, specified by ω. Rather, the $(2\theta, \eta, \omega)$ triplets[2] for each symmetrically equivalent Bragg reflection, (hkl), encompassing the set of Debye–Scherrer rings measured can be precalculated for each candidate orientation as a function of crystal space group and X-ray wavelength. Once a set of candidate indexed orientations is obtained, then local corrections to the angular coordinate systems can be performed for each grain using the current estimate of its centroidal coordinates; in other words, the effect of a precessing origin (with the sample rotation angle ω) for the local grain reference frame can be accounted for, which increases the accuracy of the measured $(2\theta, \eta)$ components for each indexed $\mathbf{G}_{hkl}$. A complete description of the geometric model for ff-HEDM is beyond the scope of this review. We direct the reader to References 30 and 36 and to J.V. Bernier (manuscript in preparation) for more detailed expositions, as well as Reference 130.

2.3.2. Bragg peak intensity modulation. In the ff-HEDM configuration, the detailed extent and morphology of the intensity distribution around each Bragg peak are affected by both instrumental and material properties. Factors that give rise to angular divergence in the diffracted beams dominate in the context of ff-HEDM. Instrumental effects include energy spread (and possibly chromatic aberrations) and angular divergence in the incident X-ray beam, point spread and pixelation in the detector, and polarization effects resulting from the rotation of the sample. The most salient material effects include intragranular gradients in orientation and strain, arising from both intergranular interactions and intragranular defect content. Pagan & Miller (33, 34) provide a detailed exposition of the anisotropic effects that intragranular orientation gradients have on the Bragg peak morphologies for different $\mathbf{G}_{hkl}$, including a method for using this information to

[2]There are actually two or no solutions satisfying the Bragg condition for each (hkl) in the rotation method, representing the intersection of $\mathbf{G}_{hkl}$ with the Debye–Scherrer cone defined by the vector equation $\hat{\mathbf{k}}_i \cdot \hat{\mathbf{G}}_{hkl} = -\sin\theta$, where $\hat{\mathbf{k}}_i$ is the unit incident wavevector, $\hat{\mathbf{G}}_{hkl}$ is the unit RLV, and θ is the Bragg angle.

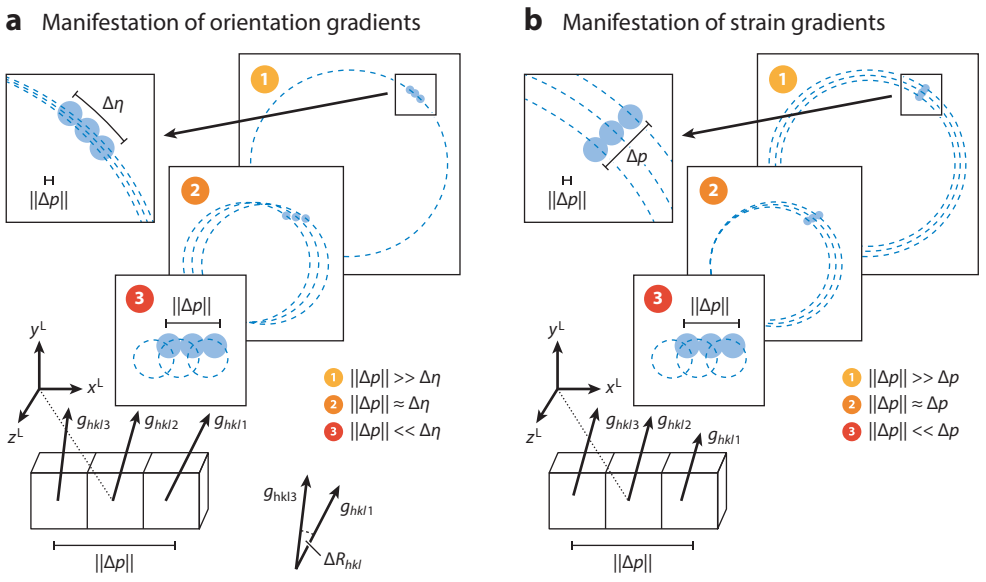

Figure 9

Schematic illustration of the relative effects of (*a*) intragranular orientation and (*b*) strain gradients as a function of detector position. Positions ① and ③ represent a near-field and a far-field high-energy diffraction microscopy configuration, respectively. Position ② represents an intermediate distance where the sample/grain-size effects and angular divergence effects are roughly equal. Figure adapted with permission from D.C. Pagan.

determine slip system activity associated with plastic deformation. **Figure 9** illustrates the gross effects of intragranular orientation and strain gradients on Bragg peak extent. An important aspect of ff-HEDM is that—to a good first approximation—orientation gradients are manifest as azimuthal-intensity modulation (η), while strain gradients are manifest as normal-intensity modulation (2θ), with respect to the reference Debye–Scherrer rings. The latter fact connects directly to Bragg's law, considering that local gradients in strain effectively alter the interplanar spacings in the crystal lattice and, hence, the Bragg angles (Equation 1). We note that for large enough (deviatoric) strain magnitudes, there is an appreciable effect on the both the interplanar spacings and the associated angles of the plane normals (**Figure 6**). However, for the limit of small (elastic) strains, which constitute the majority of HEDM studies of metals, the 2θ modulation dominates. In the ff-HEDM limit, the effect of grain precession is manifest as a harmonic translation in ω of the full set of Bragg peaks $\mathbf{G}_{bkl}$ for a grain. Grain morphology has no recoverable effect on the Bragg peak morphologies, but the relative intensities (integrated) do scale with the grain volumes.

In the context of canonical ff-HEDM analysis, the Bragg peaks are assumed to be approximately Gaussian in character; in other words, the center of the intensity distribution defining a Bragg peak can be accurately quantified and subsequently used to encode the measured $\mathbf{G}_{bkl}$ components. The accurate reduction of the measured intensities to $\mathbf{G}_{bkl}$ components is the cornerstone of the prevailing grain parameter–fitting methods in ff-HEDM (see Section 3.2). In the case of large orientation gradients, the distribution of intensities within the Bragg peaks can become markedly heterogeneous and non-Gaussian in character. These intensity variations can be interpreted using an intragranular orientation distribution function employing methods analogous to quantitative texture analysis (31, 32). Higher-angular-resolution analogs to ff-HEDM have been developed to measure these distributions to very high resolution (37–41). Note, however, that

ff-HEDM and its higher-angular-resolution analogs do not provide any spatial information for these intragranular fields.

2.4. Near-Field High-Energy Diffraction Microscopy

Traditional nf-HEDM measurements use a line-focused X-ray beam to illuminate a thin-sample cross section rather than the box beam that is standard for far-field measurements. Data from a series of cross sections (or layers) with the sample displaced perpendicular to the beam plane are collected to probe a 3D volume of microstructure. Rationalization for this protocol is given below. Recent research (130) has accelerated data collection by using a somewhat expanded box beam [essentially moving in the direction of diffraction contrast tomography (42)] so that a finite volume can be probed using a reduced number of sample rotations and associated diffraction images. This "box beam" nf-HEDM variant can be particularly useful for studying materials with large grains and/or low levels of plastic deformation where significant peak overlap is less of a concern. We focus on the more generally applicable line-focused method herein.

In nf-HEDM data collection, a high-resolution imaging detector is placed only a few millimeters (typically 5 to 15 mm) downstream of the sample, which is centered on the rotation axis (**Figure 10**). With small diffraction angles due to high energies and this small propagation distance, diffracted beams strike the detector at positions determined by both their positions of origin and the diffracted beam propagation direction, rather than falling on or near well-defined Debye–Scherrer rings, as in the ff-HEDM case. Furthermore, in the case of well-annealed samples (with single-crystalline grains), neighboring volume elements (voxels) within each grain give rise to parallel propagating diffracted beams (generated at the same ω angle) that generate a projected image of the diffracting grain cross section. The extended diffraction spots appear at seemingly random positions on the detector (**Figure 11**), so indexing peaks is far from straightforward. Furthermore, the projections of grain cross sections are highly anisotropic: Regarding **Figure 10**, peaks that scatter within the beam plane with $\eta = \pm\pi/2$ project to lines on the detector, while those scattering out of the incident beam plane have compressed but finite vertical extent. Only beams diffracted through $2\theta = \pi/2$ with $\eta = 0$ (which are never seen) would generate a one-to-one image of the grain cross section. The observed projections have extents that are qualitatively similar to the cross-section dimension perpendicular to the incident beam propagation direction but yield only low-resolution information about the dimension parallel to the beam propagation direction. Thus, individual near-field images provide surprisingly little information.

In contrast to individual images, a set of near-field images, each spanning a small $\delta\omega$ interval and collectively spanning $\Delta\omega$ of 180° or 360°, encodes extensive microstructural detail. As the sample rotates, Bragg peaks associated with many different $\{hkl\}$ for each illuminated orientation—having distinct associated $(2\theta, \eta, \omega)$—are generated; peaks from each orientation appear at least every few degrees. At each ω position, the so-called good-resolution projection direction is rotated in the sample frame of reference since it remains fixed in the laboratory. Inclusion of data spanning 180° or 360° yields isotropic shape resolution. The positions of observed spots precess with sample rotation according to their position of origin in the sample (in addition to motion due to the different diffracted beam directions specified by 2θ and η in **Figure 10**).

Determining the crystal orientation field that generates a complete set of near-field detector images is a computational challenge. The Suter group (10, 43) has pursued a forward modeling approach for this reconstruction process in which scattering from trial orientations at a given sample location is simulated so as to mimic the experimental protocol and geometry; the orientation that generates Bragg scattering (assuming a given crystal structure) that best matches experimentally observed intensity is assigned to the given location. A confidence or completeness parameter,

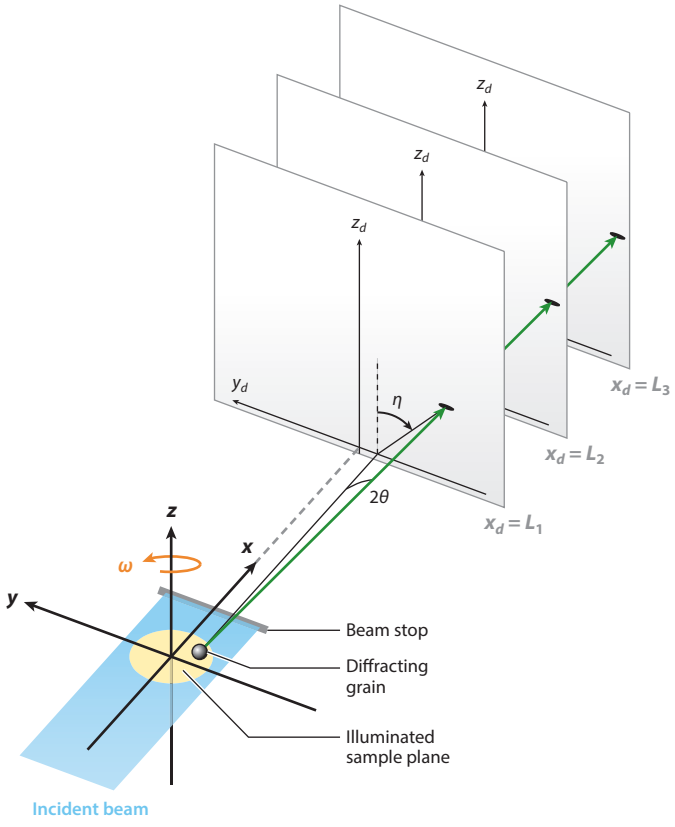

Figure 10

Schematic of a standard near-field high-energy diffraction microscopy experimental setup. The line-focused beam (*blue*) illuminates a thin-sample cross section with millimeter dimensions (*light yellow*). A single grain (*black sphere*) is indicated to satisfy a Bragg condition and gives rise to a diffracted beam (*green*). The circular grain cross section gives rise to an elliptical diffraction spot on the imaging detector (*light gray panels*). As the sample is rotated in ω, images are integrated over intervals, $\delta\omega$; sets of images span total rotation ranges of $\Delta\omega$. The measurement is repeated at two distinct rotation axis–to–detector distances, L. The laboratory coordinate system shown is consistent with the convention used at the Advanced Photon Source.

$0 \leq \mathcal{C} \leq 1$, is defined as the fraction of simulated Bragg peaks that overlap the experimentally observed intensity. Performing this optimization over an array of points or area elements determines the entire orientation field. While this approach is entirely brute force, it takes advantage of all detector data in determining each orientation. It is adaptable to a wide variety of grain sizes and sample states because it makes no assumptions about the nature of a grain other than that it assumes Bragg scattering from each reconstruction element or voxel (which is typically simulated as either a point or an area element much smaller than the grains in a particular sample). The reconstruction can start with no knowledge of the orientation field or use input from sources such as far-field data sets or previously reconstructed neighboring layer structures. Multiphase materials can be reconstructed through successive runs on the basis of different crystal structures; in each voxel, the material phase with the largest $\mathcal{C}$ is then chosen. Once a voxel orientation is determined, neighbors can begin by testing the same and similar orientations in order to take advantage of orientation correlations associated with grain structure. Current computer codes are discussed in Section 3.3.

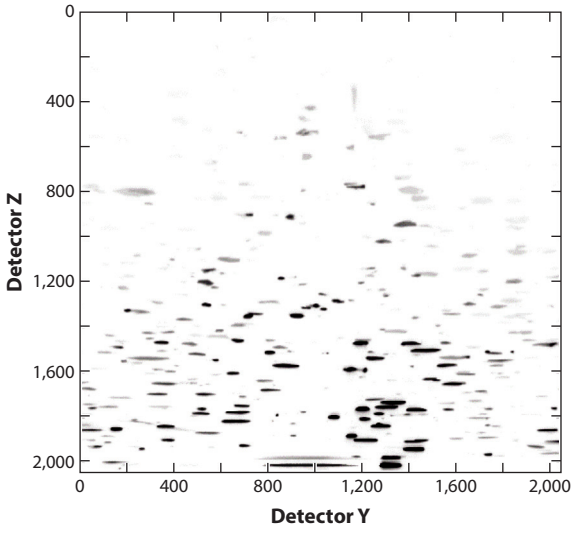

Figure 11

An example of a near-field high-energy diffraction microscopy detector image (12). The **Y** and **Z** detector coordinates are shown in **Figure 10**. Background-subtracted intensity is shown in grayscale. The incident beam projects to the dark line at the bottom with a small amount of stray scattering from the beam block just above. While a few artifacts are present, most intensity features are diffraction spots from the ordered zirconium crystalline grains. The horizontal extent of the vertically compressed projected images of grains are indicative of grain cross-section dimensions in the range of roughly 20 to 150 μm. Units are in 1.5-μm-pixel numbers. The image was collected as the sample was rotated through $\delta\omega = 1^\circ$.

A critical initial step in the reconstruction process is the segmentation of detector signals from backgrounds due to readout noise, stray scattering, and so forth. For forward analysis, this process does not have to separate individual diffraction signals from one another but rather only needs to separate signal from background. Inclusion of sparse isolated random signals will have little effect on reconstructions since these are unlikely to recur appropriately on images taken at multiple distances and/or at appropriate rotation intervals to mimic Bragg scattering. In contrast, the determination of diffraction signal shapes is crucial: The reconstruction is essentially a pattern matching process based on projections. The intensity pattern within grain projections is, to first order, determined by the geometry of the cross section, as the intensity in a pixel is determined by the volume of material that scatters into it. This also emphasizes that pixel intensities in spatially resolved projections are independent of the total grain size. Intensities from edges and corners of grains tend to be reduced due to associated restricted material volumes. Since cross-section edges and corners correspond to parts of grains that are close to grain boundaries and higher-order junctions, which are important microstructural features, the reconstructions should not be biased by the reduced intensity but should reproduce the entire projection. Therefore, our forward model codes ignore the intensity, and our image analysis attempts to include weak as well as strong regions. Current practice is discussed in Section 3.3. Intensity patterns do, of course, contain salient information, and we briefly discuss efforts to extract that information below.

Internal microstructural features in well-ordered microstructures can be resolved to at least the raw detector pixel resolution or intrinsic point spread width (44). This implies that, through the observation of many Bragg peaks from each orientation, the pattern extraction from detector images such as that in **Figure 11** accurately reproduces grain cross-section projections and that

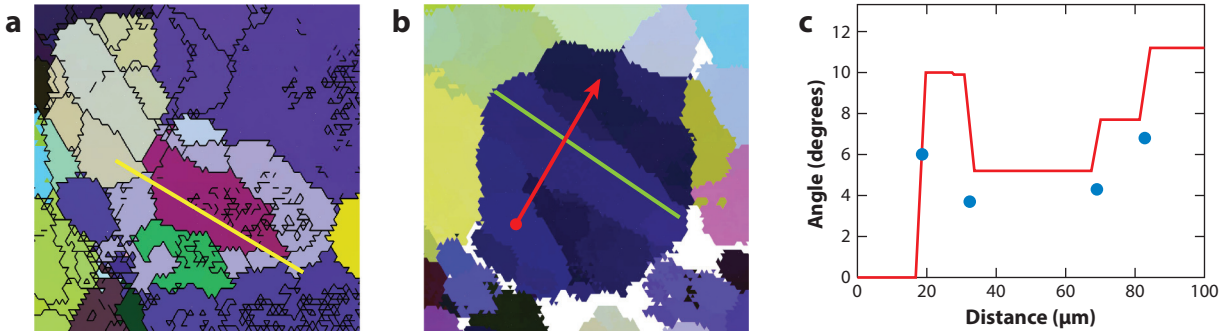

Figure 12

Near-field high-energy diffraction microscopy reconstructions showing responses to plastic deformation in a zirconium polycrystal sample. The sample was loaded in uniaxial tension to 13% engineering strain. In panels *a* and *b*, spanning 150 × 150 μm^2 and 200 × 200 μm^2, respectively, colors are mapped from Rodrigues vector components specifying unit cell orientations. (*a*) A region showing twin formation. Central dark red and green regions are distinct twin variants related to the originally uniformly oriented light blue parent grain. Note the light gray/cream-colored region (*upper left*), which was formerly a single grain but now contains a rotated region spatially connected to the red twin in this and adjacent layers. To the left of the twinned grain is a light brown grain with a slightly misoriented gray grain within it, suggesting that the twin activity in the neighbor grain influenced the dislocation activity in that grain. Black lines between neighboring voxels with $\geq 1^\circ$ highlight the orientation gradients within grains developed by plastic deformation. (*b*) The dark blue grain exhibits orientation discontinuities with rotations about axes close to the local *c* axis as expected in prismatic slip events. (*c*) The red line shows the rotation angle relative to the starting point as one moves along the red arrow in panel *b*. Blue points show the tilt of the rotation axis away from the local *c* axis. Panel *a* adapted from figure 2*e* of Reference 12. Panels *b* and *c* adapted from Reference 70.

inevitable edge determination noise is signal averaged in the reconstruction process (45). For voxel positions near grain boundaries or other features, there is a natural competition between multiple orientations; that is, due to imperfect spot shape determination, more than one orientation may produce a local maximum in $\mathcal{C}$. Note that this competition is difficult to see on the detector images because completely different sets of peaks are involved in the distinct orientations. Nevertheless, picking the orientation that maximizes $\mathcal{C}$ is empirically observed to yield accurate feature locations. That this remains true even in somewhat deformed materials is strongly implied by the structure shown in **Figure 12**.

As shown above, both nf- and ff-HEDM have been applied to deformed states of materials as well as to pristine, ordered states containing single-crystalline grains. Deformed materials exhibit orientation gradients and discontinuities within what would commonly be referred to as grains. These orientation variations are commonly referred to as mosaic structure, implying that there are local single-crystalline regions that are misoriented relative to their neighbors; continuous lattice bending may also appear at mesoscopic length scales. While the breakup of grains, as illustrated by twinning in **Figure 12**, generates new, well-separated, spatially resolved peaks, closely spaced or continuous orientation variations generate diffraction peak broadening in η and ω (transverse broadening in reciprocal space). In far-field images, spots broaden along Debye–Scherrer rings and appear in successive ω intervals. Grains become ill defined since an arbitrary misorientation threshold must be used to select regions of similar orientation. Furthermore, deformed (as well as some undeformed) materials exhibit unit cell distortions (elastic strains) due to internally or externally applied stresses.

In the near field, rotation-induced broadening means that intensity patterns are no longer simple projections of grains. However, as long as each sample space voxel has a well-defined orientation, the set of ~100 observed diffraction conditions is constrained to rotate in a consistent way and to maintain its position of origin. In this sense, the reconstruction problem is unchanged,

but the effective grain size has been reduced (which can result in a dramatic increase in computation time required). As is demonstrated in Reference 10 and consistent with Reference 8, the forward model method degrades gracefully as orientation variations increase. This behavior has been useful in several applications (9, 12, 14, 15, 17, 46). Very broad distributions associated with highly deformed states generate very broad scattering with severe overlap of signal from disparate sample regions and make reconstructions ambiguous.

While ff-HEDM extracts grain- or cross-section-averaged elastic strain states through precise measurements of diffraction spot positions on the detector, nf-HEDM lacks sufficient resolution in scattering angles for such analysis. However, research is under way to develop the ability to deduce strain tensors (with reduced resolution) in selected cases on a voxel-by-voxel basis by observing splitting of diffraction spots between detector images. This research will be reported in a future publication (Y.F. Shen, H. Liu, C. Zhang & R.M. Suter, manuscript submitted).

3. IMPLEMENTATION

In this section, we present details of the implementation of HEDM techniques, with a focus on the 1-ID-E instrument at APS. Topics include a summary of the hardware from source to detectors, data collection protocols, data handling, reconstruction software, output formats, and postreconstruction data analysis. A new HEDM instrument has recently been implemented at the 6-ID-D end station of the APS, with similar characteristics but with a variety of hardware and software upgrades.

3.1. Beamline and Hardware Requirements

HEDM measurements are data intensive due to the large numbers of diffraction images required; they therefore benefit from high fluxes of high-energy X-rays so as to accelerate image detection. In some cases, speed is limited by detector readout times; in others, by signal accumulation or exposure times.

3.1.1. Source and front end. High-energy X-rays at 1-ID are produced by a superconducting undulator source (47). A bent double-crystal monochromator allows continuous coverage over the range $42 < E < 120$ keV with a band pass of $\Delta E/E \sim 1 \times 10^{-3}$, resulting in fluxes of 6×10^{12} photons per second at 80 keV (full beam of 1.5 horizontal $\times$ 1 vertical mm^2 at the sample position) (21). For higher-q-resolution studies, a secondary four-bounce flat silicon monochromator can be used to reduce the band pass to below 1×10^{-4}, with concomitant flux loss.

3.1.2. Optics and beam geometries. The 1-ID beam is delivered to the E hutch, which is located 75 m downstream of the source (at the sample location). Tantalum slits with a thickness of 5 mm are used to define the beam size at the input to the apparatus. Refractive optics can be used to produce 1D or 2D focused beams, with large focal lengths (2 m or more) such that beam divergence is below 150 μrad, providing sufficient $\boldsymbol{Q}$-resolution for standard HEDM measurements (21). For nf-HEDM, the standard optical configuration is a vertically line-focused beam (~2 μm FWHM high) and a horizontal size up to 2 mm, as determined by another set of high-energy slits. This configuration yields an ~100-fold-enhanced flux relative to that of an unfocused beam of similar dimensions. The line-focused beam allows for illumination of virtual slices of samples up to ~1.5 mm in diameter.

Far-field measurements typically use a box beam that is defined by the second set of slits with the refractive lenses out of the beam. In this way, an entire volume of material can be probed with a single ω-rotation scan. The vertical extent of the beam can be as large as ~0.5 mm, so

the illuminated volume can be large; in practice, the vertical extent is chosen so that detector images are not so highly populated by diffraction spots as to generate overlapping peaks along the Debye–Scherrer rings. In some cases, far-field data have been collected using the same line-focused beam as for near-field measurements (18); this allows averaged elastic strain states to be resolved (on a subgrain level) in each cross section with well-defined grain geometries from the near-field measurement.

3.1.3. Sample positioning and rotation. For most HEDM measurements, samples are placed on a six-axis stage stack, the heart of which is a high-resolution (air-bearing) rotation stage (Aerotech ABRS300) with a vertical rotation axis (this rotation corresponds to the ω variable in **Figure 10**). Since the rotation axis is perpendicular to the incident beam, the illuminated sample volume is independent of the ω rotation. Above the ω stage are three translation and two tilt stages for positioning different sample volumes relative to the rotation axis.

Additional equipment (furnaces, small load frames, etc.) can be placed on or next to the sample mounting stack for in situ measurements, with several exemplary cases presented in Section 4. More sophisticated equipment that is compatible with both nf- and ff-HEDM measurements has recently been developed and includes an in-grip rotational and axial motion system (RAMS) (29, 48) and biaxial loading (49). There are currently RAMS variants installed at both CHESS and APS that provided unobstructed sample rotation over a full 360° with 4 kN axial load capacity at rotation rates of up to 60° per second. Recent upgrades provide torsional loading capability, which was successfully tested at APS in August 2019. Furnaces compatible with ff-HEDM are available for thermomechanical studies [e.g., Pagan et al. (72)], and a smaller nf-HEDM-compatible furnace has been developed.

3.1.4. Computational infrastructure. Management and processing of the majority of the high-energy X-ray data described herein are currently handled by the APS Data Management System (50, 51). This system allows data to be efficiently and securely stored and piped to the appropriate algorithms for reconstruction. Similar efforts are under way at other facilities, including the Diamond Light Source (see **https://icatproject.org/**) and the National Synchrotron Light Source II (52). These facilities' data management systems have similar goals, but they have been customized and developed to address the unique needs of each facility. Common goals include faster (up to real-time) data analysis and visualization (particularly for in situ experiments) and efficient data storage (e.g., through data compression) and handling of (both X-ray and external) metadata. Current infrastructure at the APS includes a Data Direct Networks storage appliance with 3.6 PB of usable storage, which connects to an InfiniBand switch. Data transfer nodes with speeds up to 40 Gbps link the storage to the beamline network as well as to the Argonne Leadership Computing Facility (ALCF). Computing resources used to reconstruct and visualize HEDM data include the ALCF, local and users' clusters, and other leadership computing centers [e.g., Extreme Science and Engineering Discovery Environment (XSEDE) and National Energy Research Scientific Computing Center (NERSC)].

HEDM information in a set of 360 to 3,600 detector image files must be converted into a map of unit cell orientations and associated data. Several projects have developed codes based on several different approaches and algorithms (**Table 1**).

3.2. Far-Field Requirements

Here we present the essential requirements of a ff-HEDM instrument implementation and data collection scheme. While this is by no means an exhaustive description covering all variants, we

Table 1 Overview of the various reconstruction codes for HEDM data

Code name	Origin	URL	nf-HEDM	ff-HEDM
Fable[a]	ESRF/Risø/DTU	**https://sourceforge.net/projects/fable/**	✓[b]	✓[c]
IceNine	CMU/LLNL	**https://github.com/FrankieLi/IceNine**	✓	
HEXOMAP	CMU	**https://github.com/HeLiuCMU/HEXOMAP**	✓	
hexrd[d]	LLNL/CHESS	**https://github.com/HEXRD/**	✓	✓
MIDAS[d]	APS	**https://www.aps.anl.gov/Science/Scientific-Software/MIDAS**	✓	✓

[a]Fable is a collection of several different software projects that provide specific functionalities.
[b]Grainsweeper3d.
[c]ImageD11, Grainspotter (58), FitAllB (53).
[d]The hexrd and MIDAS projects are self-contained.
Abbreviations: APS, Advanced Photon Source; CHESS, Cornell High Energy Synchrotron Source; CMU, Carnegie Mellon University; DTU, Danish Technical University; ESRF, European Synchrotron Radiation Facility; ff-HEDM, far-field HEDM; HEDM, high-energy diffraction microscopy; LLNL, Lawrence Livermore National Laboratory; nf-HEDM, near-field HEDM.

provide the common hardware and currently available measurement timescales (i.e., at a third-generation synchrotron source) for reference. We also provide fundamental descriptions of the data analysis, specifically orientation indexing and grain parameter refinement. We recognize that different algorithms exist for these purposes, and have made an effort to focus on the data character in an algorithm-agnostic manner.

3.2.1. Hardware. The ff-HEDM detector is a large flat-panel detector with ideally little to no spatial distortion. Typically, a GE 41RT detector is used and cocentered with the direct beam. Other detectors (e.g., Dexela 2923, Pilatus 2M CdTe) can also be used; these offer faster speeds and/or dynamic range but have limitations because they are paneled detectors, so there are gaps in q-space coverage (due to dead space between panels) and somewhat higher spatial distortions. Multidetector configurations are also possible (for example, 1-ID uses four GE 41RT detectors) arranged about the direct beam to create a large effective detector (also with gaps in q-coverage due to finite detector edges). Typical ff-HEDM sample-to-detector distances range from 0.5 to 3 m, with shorter distances for single detectors and larger distances for the four-detector configuration. As a result of the higher detection efficiency, ff-HEDM can be performed up to ∼100 times faster than nf-HEDM, such that detector speed often limits ff-HEDM exposure rates (with GE 41RT down to 0.2 s), whereas nf-HEDM exposures are typically flux limited and range from 0.3 to 5 s. Finally, at the downstream end of the hutch (∼5 m from the sample) an area detector (e.g., Pixirad-2 CdTe) can be placed on a translation–rotation assembly to carry out very far-field HEDM measurements with q-resolution sufficient for reciprocal space mapping of individual diffraction spots (37, 38, 40).

3.2.2. Data collection. For the best results in analysis, ff-HEDM measurements should be conducted using the full 360° rotation range (36, 53). In particular, the accuracy of the strain and centroid improves with the observation of the same $\mathbf{G}_{hkl}$ at different sample orientations. The typical oscillation interval employed is $\delta\omega = 0.25°$; however, smaller intervals are possible with increasing detector framing rates. The angular extent of the diffraction spots sets an upper limit on the appropriate $\delta\omega$; note that the accuracy of the measured centroid of a Bragg peak improves with finer sectioning. Data are typically collected by utilizing a flying scan during in situ measurements, in which the sample is rotated continuously while the detector integrates signal and reads

out data. There is a trade-off between (*a*) the desire to measure a full volume quickly enough that the sample state does not change appreciably between the beginning and end of the rotation and (*b*) the fact that the finite readout speed of the detectors creates spatially dependent distortions in the ω value for each pixel in a single exposure that increase with the rate of rotation. With the GE 41RT detectors, it is possible to measure a full 360° sweep in ~30 s. The associated data rate is ~400 MB/s for each 2,048 × 2,048 detector. The newest Eiger detectors have the potential to run nearly three times faster with more than four times as many pixels per detector. In general, a major limiting factor for data collection in ff-HEDM is the limited dynamic range of conventional integrating detectors; it limits the ability to measure samples with a broad range of grain/domain sizes without either oversaturation (for the large grains) or falling below the detection threshold (for the small grains). Many studies concerned with twinning and/or phase transformations embody this challenge. The latest generation of large-format detectors (e.g., Pilatus and Eiger) marry smaller pixels, single-pixel point spread, and high dynamic range at very high photon count rates. These currently available advances in detector technology stand to significantly advance the implementation of ff-HEDM.

3.2.3. Orientation indexing. At the most fundamental level, the indexing step can be viewed as the segmentation of orientation space to identify which crystallographic orientations are consistent with diffracted intensities on the detectors; orientation is the key that maps a grain orientation to the general locations of the associated Bragg reflections in the diffractogram. In macromolecular crystallography, the indexing step involves solving for both the space group and crystal orientation, and the fitting step is focused on retrieving integrated Bragg reflection intensities to perform structural analysis. By contrast, the space group(s) of all phases present is typically known a priori in HEDM, which greatly expedites the data reduction complexity; we note, however, that Wejdemann & Poulsen (54) have demonstrated a method for indexing unknown phases in the context of ff-HEDM, though at considerable computational cost. The additional complication in ff-HEDM versus macromolecular crystallography is the polycrystalline nature of the sample, which necessitates deconvolution in the indexing procedure.

Most of the strategies used to address this issue ultimately involve some form of direct search in the orientation space. This is illustrated by way of the simplest—but generally least efficient—approach to indexing: an exhaustive search in orientation space in which the validity of each orientation is tested by using a forward projection onto the diffractogram space. By simulating all of the Bragg reflection locations in the diffractogram coordinates, the test reduces to a local signal detection problem using boxes with appropriate tolerances in $(\mathbf{X}_d, \mathbf{Y}_d, \omega)$. Alternatively, the local pixel intensities can be interpolated onto a local grid of angular coordinates $(2\theta, \eta)$. The local detection of Bragg peaks can be simple (e.g., applying a threshold and connected components labeling) or complex (e.g., applying a feature detection algorithm). Each orientation can be assigned a scalar weight that represents the ratio of detected signals to expected signals. This ratio is alternately referred to as completeness or confidence in the 3DXRD and HEDM literature. Orientations above a minimum completeness threshold constitute the candidate grain orientations for the volume probed in the rotation series. Ideally, the threshold would be unity; however, practical limitations imposed by factors such as heterogeneous grain-size distributions, phases with vastly different scattering cross sections, limited dynamic range of the detectors, fluctuations of incident intensity, and other measurement errors generally require relaxation of the completeness threshold to 75–90%. Setting the threshold too high runs the risk of systematically biasing against smaller and/or more weakly scattering grains. Conversely, setting the value too low can lead to spurious indexing results. The candidate grain orientations can optionally be clustered using the minimum misorientation threshold to produce a final indexed set of orientations.

This indexing procedure is robust but generally slow, as $\mathcal{O}(10^6$–$10^7)$ orientations are needed to span orientation space at a sufficiently fine resolution. There are several means by which the orientation search can be optimized. For example, the tests for each candidate orientation in the search space are independent, which allows straightforward parallel processing to be applied. Adaptive searches at increasing resolution (e.g., 10) can also significantly increase efficiency. However, the geometry of ff-HEDM combined with the negligible effects of precession and strain (in most cases) enables a dimensional reduction that can substantially expedite the indexing process.

Note that in using the term "measured Bragg peak" in the previous paragraph, we imply that the measured intensities comprising a single Bragg reflection can be identified in the raw data. Indeed, most prevailing analysis methods begin with the application of segmentation or feature detection either globally or locally (e.g., in the vicinity of Debye–Scherrer rings only) to the 3D diffractograms to isolate signal (Bragg peaks) from background. A plethora of image processing tools and techniques exist for this data reduction step, which results in the distillation of the full diffractogram data (i, j, ω, I) to a list of $(i, j, \omega) \rightarrow (2\theta, \eta, \omega)$ triplets that encode the measured Bragg peaks. The intensity information is largely ignored in most indexing procedures after segmentation. The notion that the data can be reduced in this way, however, raises another limitation of the ff-HEDM technique: The nature of the Bragg reflections must be reasonably compact and quasi-Gaussian in order to accurately associate the intensity distributions in the raw data to a single peak. When the Bragg reflections exhibit marked heterogeneity, as is the case in the presence of large gradients in intragranular strain and/or orientation, a different analysis modality must be applied (see References 31 and 32 for examples). Furthermore, if a significant fraction of the Bragg peaks are overlapped, the traditional ff-HEDM analysis methods break down. The incidence of signal overlaps increases roughly linearly with the number of distinct grains (i.e., spatially separated and above the intergranular misorientation threshold) in the diffraction volume, and roughly quadratically with the angular spread of the individual Bragg reflections (arising mainly from large intragranular misorientation) (30).

Given a set of reduced diffraction peaks, each is associated with an underlying orientation fiber (up to degeneracy),

$$\mathsf{R}(\phi)\mathbf{c} = \pm\mathbf{s}, \qquad 4.$$

where $\mathsf{R}(\phi)$ is the one-parameter set of crystallographic orientations that leave the crystal-based vector $\mathbf{c}$ parallel with the sample-based vector $\mathbf{s}$. In the current context, $\mathbf{c}$ represents a unit RLV (i.e., lattice plane normal) and $\mathbf{s}$ represents a unit scattering vector in the sample frame for which a Bragg condition was recorded. We note that this procedure is completely analogous to pole figure measurement and subsequent inversion in texture analysis (32, 55). Having knowledge of the orientation fiber is immensely useful for indexing, since the orientation of the crystal from which the associated Bragg peak emanated must be along this 1D contour. Furthermore, the set of orientation fibers underlying all of the Bragg peaks for a single grain mutually intersect at exactly one point in the orientation space: the underlying grain orientation. This fact can be exploited in the indexing procedure, and there are various means by which these knots in the orientation fibers can be found. **Figure 8*b*** shows a collection of such knots for a cubic ($m\bar{3}m$) material. Using, again, the example of a direct search indexing strategy, an exhaustive 3D search in orientation space may be replaced by a collection of 1D searches on the fibers generated from the reduced data, which can be much more efficient. While it is possible to envision an indexing procedure cast as an inverse problem using a forward model—analogous to pole figure inversion (32, 55)—the computational requirements and difficulties in representing the sparsely populated orientation space at sufficiently high resolution have conspired to preclude any development along these lines.

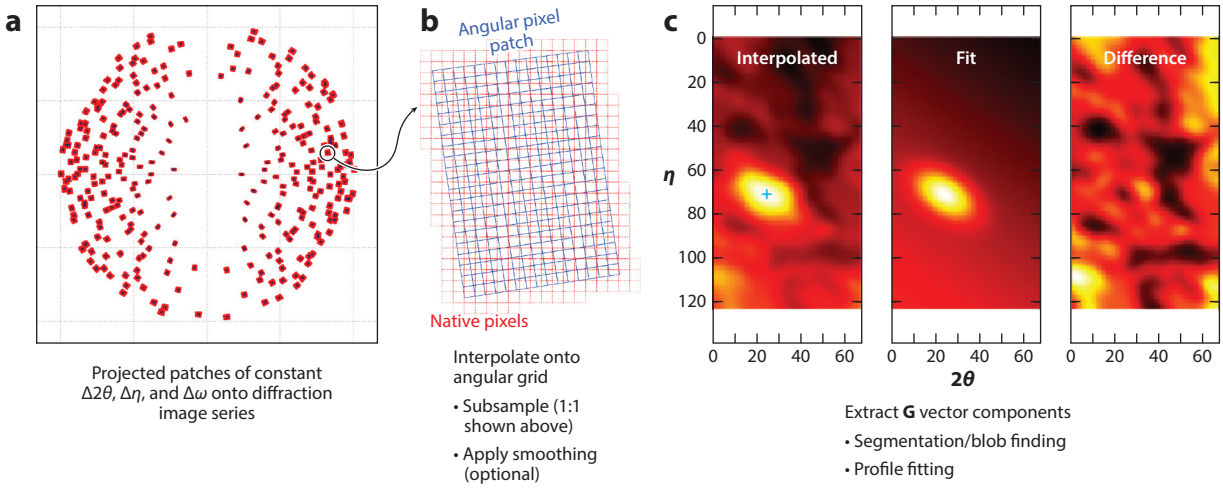

Figure 13

A schematic of the local interpolation of intensities for each predicted $\mathbf{G}_{hkl}$, and subsequent reduction of the intensity data to $\mathbf{G}_{hkl}$ components. The example is shown in two dimensions for clarity.

Several different search-based indexing methods, however, have been developed, validated, and implemented in software packages, which we list in **Table 1**.

3.2.4. Signal extraction and intergranular parameter fitting. The indexing procedure provides a list of crystallographic orientations that are consistent with the measured intensities; these values are approximate but serve as keys to the raw data that yield the nominal locations of the Bragg reflections associated with each orientation (i.e., grain). Those locations span the entire diffractogram (**Figure 5**). Each Bragg reflection, in turn, comprises a distribution of intensities in the diffractogram, as described in Section 2.3, above. The breadth and structure of those distributions are sensitive to instrumental parameters, such as energy bandwidth, beam divergence, and detector point spread, as well as to intragranular gradients of orientation and strain.

A simple approach is to reduce the diffractogram to a list of $\mathbf{G}_{hkl}$ components by using segmentation or more complex feature extraction (45, 56). Depending on the approach, the center, intensity, and higher-order moments of the Bragg peaks may be available. This can be done globally on the full diffractogram, but that approach can become problematic in the presence of artifacts, parasitic scattering, or highly overlapped regions. A more refined and parallelizable approach is to leverage the preindexed list of candidate orientations to perform local intensity extraction for each reflection on a grain-by-grain basis. This process avoids some of the segmentation issues, such as parameter tuning, for the full image stack. By using appropriate tolerances in $(2\theta, \eta, \omega)$, one can interpolate the raw intensities onto a local angular grid for each predicted $\mathbf{G}_{hkl}$ (**Figure 13**). These locally interpolated intensity profiles are used to yield $\mathbf{G}_{hkl}$ components via either feature extraction or profile fitting—there are many options for this process. Once the measured intensities have been reduced to a list of $\mathbf{G}_{hkl}$ components, the parameters for grain orientation, centroidal position, and strain can be estimated via an optimization problem (e.g., nonlinear least squares). The parametric model that takes a reference list of $\{hkl\}$ and computes the associated $\mathbf{G}_{hkl}$ components is nonlinear. The different ff-HEDM reduction codes employ different variations on the parameterizations for the orientation and strain (or stretch), but all solve analogous optimization problems to match simulated with measured $\mathbf{G}_{hkl}$ components directly, or with their angular

representation ($2\theta_{hkl}$, η_{hkl}, ω_{hkl}) (36, 53, 57). In the latter case, the residual components may be weighted differently on the basis of the estimated uncertainties in the three angular coordinates. In particular, the magnitude of the $\delta\omega$ employed in the measurement can have a large associated uncertainty if it is on the order of a typical Bragg peak FWHM.

Following the parameter optimization, the associated residual error may be employed to calculate an effective figure of merit to assess the quality or validity of the grain. The completeness (or confidence) ratio may also be recalculated for each candidate grain by employing local signal detection in the extraction procedure. However, the use of completeness alone for ranking candidate grains can be misleading, as it is biased against smaller grains. Weighted completeness is more effective; here, only $\mathbf{G}_{hkl}$ with a relative structure factor $\geq$1–10% (for example) of the maximum are considered. Still, completeness is more effective as a gross threshold for the candidate grains that can subsequently be ranked by their goodness of fit. As mentioned above, regions containing overlapped Bragg peaks are generally associated with higher errors. These outliers can be problematic when employing a squared $\mathcal{L}2$ norm for the residual (e.g., as in least squares optimization). The frequency of these overlapped regions increases rapidly with increasing number of grains, as well as with Bragg peak breadth (30). This issue can be exacerbated significantly for samples containing a large population of twin-related domains. Therefore, it is prudent to employ strategies to identify and remove overlapped Bragg peaks from the fitting. A simple strategy is to employ an iterative fitting strategy, applying heuristics to remove outlier reflections. Overlapped, or nearly overlapped, reflections can also be quickly identified using the gross indexed orientations via a cluster analysis (J.V. Bernier, manuscript in preparation).

Looking toward the future, a particularly powerful—but computationally onerous—approach to grain parameter optimization would be to frame it as an inverse problem. This is analogous to a 3D Rietveld refinement, in which a forward model for the diffracted intensities is used to form a residual on the measured data. The recent development of hybrid CPU/GPU computational frameworks and research centers focused on realizing exascale computing may enable this approach. This not only would alleviate issues with overlapped regions but also has the potential to push the analysis of ff-HEDM data toward more heterogeneous and/or heavily deformed samples while facilitating the extraction of intragranular distributions of orientation and strain.

3.3. Near-Field Requirements

The following paragraphs describe implementation requirements of the near-field technique. Hardware and software requirements are distinct from those of the far-field method due to the required high spatial resolution needed to determine grain shapes. High-resolution imaging of high-energy X-ray beams necessarily leads to slower data collection than in the far-field case. This follows from the use of detectors with smaller pixels (1.5 μm versus 200 μm pitch or a collection area ratio of $\sim 6 \times 10^{-5}$ per pixel) and a thin (10–15 μm) scintillator needed to avoid broadening of beams incident at various 2θ angles. For nf-HEDM, the incident beam is typically focused in the vertical direction to a line. The demagnification by a factor of order 200 yields a comparable increase in beam intensity, which partially compensates for the above factors. The line-focused beam illuminates only a quasi-planar cross section of the sample. Section-by-section data collection yields the requirement of collection of many layers (typically 10 to 100) to generate 3D data sets. The line-focused beam results in 2D detector images of the 2D cross sections, which reduces the reconstruction process to pattern matching rather than requiring intensity matching. In principle, this leaves the intensity patterns available for separate analysis based on more complex scattering models. We point out below that the spatially resolved imaging technique has substantially reduced intensity (or counting time) dependence on grain size relative to

ff-HEDM and therefore senses a larger-grain-size dynamic range. In contrast to the above distinctions between the nf- and ff-HEDM techniques, the sample and sample rotation requirements are identical (as are those required for tomography). No sample manipulation is required to switch techniques.

3.3.1. Hardware. The near-field grain mapping technique requires a high-resolution imaging detector to collect accurate images of diffraction spot shapes. These shapes allow the technique to determine accurate grain cross-section shapes that can be assembled into 3D grain ensembles. With high spatial resolution comes a limitation to small fields of view, thus requiring that the detector be placed close to the sample. At 1-ID-E, the nf-HEDM detector is a home-built system designed by Lienert (24). The detecting element is a LuAG scintillator (a $\leq$25-μm-thick lutetium aluminum garnet single crystal) that produces visible scintillation light, a portion of which strikes a mirror that directs the light into a magnification optic that, in turn, focuses the light onto a CCD detector. The current system uses fivefold magnification onto a 7.3-μm pixel pitch, yielding an effective pixel size of 1.5 μm; the 2,048 $\times$ 2,048 array yields a field of view of 3 $\times$ 3 mm^2. The detector system's resolution is 1.5 μm. The detector system can be translated along the X-ray beam to vary the sample-to-detector distance, typically ranging from 5 to 15 mm. The use of an interlaced CCD allows the readout of an image while a new image is being collected, which in turn allows the sample to rotate continuously during data collection (i.e., a fly scan).

3.3.2. Data collection. As pointed out above, data need to be collected over a wide range of sample orientations in order to produce isotropic resolution of grain cross-section shapes. The typical practice is to use $\Delta\omega = 180^\circ$, which ensures that each cord across a cross section is oriented in the highest-resolution imaging direction (perpendicular to the incident beam; see Section 2.4) for an equal interval during data collection, which yields isotropic resolution of grain shapes.

In the fly scan mode of data collection, the time required to collect data for a given cross section or layer is determined by the rotation speed, $\dot{\omega}$. If a Bragg peak has an intrinsic width in ω, given by $\delta\omega_B$, which is less than the angular range for image collection, $\delta\omega$ (which is typically true for ordered grains), then the intensity is proportional to $\delta\omega_B/\dot{\omega}$. Unfortunately, $\delta\omega_B$ depends strongly on the scattering geometry, varying as $1/\sin\eta$ (with a resolution-dependent cutoff at small η) (**Figure 10**).

This strong variation is on top of structure dependencies such as the structure, form and Debye–Waller factors, and additional parts of the Lorentz polarization factor. In practice, $\dot{\omega}$ has to be determined at the beamline for each measurement and has to be a compromise between collecting strong statistics and not taking too long for each scan. With the current conditions at 1-ID, typical rotation rates of order 1° per second yield 3 min per scan, 6 min per layer, or 17 layers per hour; volumetric data sets may probe 100 layers and require 6 h. The CCD camera reads out at a maximum rate of 0.3 s per image, so $\delta\omega \geq 0.3^\circ$. This typical estimate implies that the measurement time is limited by the readout time rather than detector efficiency and incident flux. In contrast, for weakly scattering materials or deformed states of materials, $\dot{\omega}$ must be reduced in order to obtain reasonable statistics, and then the measurement becomes efficiency or flux limited.

3.3.3. Reconstruction codes and outputs. For nf-HEDM, Carnegie Mellon University (CMU) codes use a forward modeling procedure (10, 11) that simulates the experimental geometry and data collection protocol as well as the sample geometry and crystal structure. Sample space is divided into discrete voxels (volume elements), and the orientation space associated with the known or assumed crystal point group symmetry is searched using a hierarchical strategy (10).

For each trial orientation, Bragg conditions on ω are computed, the relevant detector images are determined, and diffracted beams are projected from the voxel location at each ω onto the appropriate the simulated detector image; overlap is determined between simulated and experimental detector images. The fraction, $\mathcal{C}$, of simulated peaks that overlap experimentally observed intensity is evaluated. Finally, the orientation that generates the maximum $\mathcal{C}$ is assigned to the voxel, and the associated value of $\mathcal{C}$ is recorded along with orientation parameters. As described and justified in Section 2.4, this amounts to a pattern matching process that ignores intensity variations within or between the peaks. Note that this procedure uses the entire data space associated with each orientation to optimize each voxel orientation rather than back-projecting individual Bragg peaks. While it is assumed that the structure within each voxel or resolution element is single crystalline, there is no further assumption of crystallinity. Thus, a broad range of grain sizes can be extracted, and significantly deformed materials can be analyzed. After reconstruction, grains can be identified by collecting sets of contiguous voxels that have similar orientations. The steps involved in the reconstruction process are described below.

3.3.3.1. Diffraction signal extraction. Raw detector images contain bright regions corresponding to diffracted beams but also have a variety of artifacts generated by stray scattering (especially generated by the nominally single-crystalline tungsten beam stop) and stray visible light. A somewhat uniform background from readout noise is also present. Most of these backgrounds are independent of time and of ω, so we generate and subtract a median image (or images), which is the median intensity in each pixel over an entire 180° rotation or some other large range. As long as the selected range is large compared with the persistence range of diffraction spots, the difference between the raw images and the median will contain only diffraction signals. The use of less than 180° can be appropriate if there is a slowly varying (in time or ω) component in the background that is clearly not due to diffraction. Difference images still contain low-level noise at the pixel-to-pixel level with some negative numbers included. Negatives are set to zero, and a uniform subtraction (typically 0–10 counts but substantially less than peak intensities) can be done to eliminate this noise.

Next, a blob-finding image analysis routine is applied to identify regions with above-background signals. The remaining pixels are kept as lists of pixel addresses with the associated background-subtracted intensities. These lists are stored in binary form and are the input to the reconstruction algorithms. The binary images are a compressed form (clearly lossy compression) of the data that is typically smaller by a factor of at least 10 relative to raw images.

3.3.3.2. Inputs. In addition to the binary reduced data files generated as above, the codes require a set of parameters that describe the experimental setup, the data collection protocol, and the crystal structure to be applied. The physical detector is described in terms of the pixel pitch (pixel spacing in the array) and the number of pixels in the square array. The position and orientation of the detector are defined at each measurement position. As shown in **Figure 10**, a laboratory coordinate system is defined to have its origin at the intersection of the incident beam and the ω-rotation axis (note that this is independent of any sample location or position; also note that the assignment of axes is different from that described in Section 3.2). The input file specifies the origin of detector coordinates (j_0, k_0) as the projection along k_i of the beam intersection with the rotation axis. Displacements on the detector face are measured along pixel array directions. Physical displacements in space are modified through detector orientation parameters specified in terms of Euler angles.

An initial orientation map defines the set of voxels to be reconstructed. This set can contain null orientations or previously determined orientations (a previously reconstructed layer, a set of

orientations from a far-field measurement, a simulated or synthetic microstructure). Voxels to be reconstructed in a particular run are input with $\mathcal{C} = 0$, and above-threshold confidence (typically $\mathcal{C} = 1$) indicates voxels that will remain fixed to their initial orientation.

For IceNine, the microstructure input and output files are described in the following subsection. Reconstructions are performed on the basis of triangular area elements. The pyHEDM code will use a simple image format based on a regular grid array of points (H. Liu, C. Zhang, Y. Shen & R.M. Suter, manuscript in preparation).

3.3.3.3. Outputs.

A sequence of outputs can be generated:

- Experimental geometry. An optimized reconstruction requires optimized geometry parameters. Typical practice starts with collecting data from a small sample that has been well centered on the rotation axis. The small sample allows back projection of observed peaks (at at least two detector positions) to the position of their intersection in the plane of the incident beam. The usual practice is to use an ~50 μm gold sample (either wire or cube on a mounting support). A preliminary reconstruction of this test sample yields a map of $\mathcal{C}$. The codes generate such maps on the basis of varied experimental geometry parameters in order to determine an optimal set of parameters that yield maximum $\mathcal{C}$. IceNine uses Monte Carlo variations, while the new pyHEDM code uses a so-called twiddle algorithm (see **https://martin-thoma.com/twiddle/**). Optimized parameters are then passed to the main reconstruction algorithm.
- Reconstruction. Reconstruction proceeds with parameters determined as above. Assuming that the experimental apparatus is stable, these parameters are sufficient for an extended set of layer measurements. If $\mathcal{C}$ values drift downward in successive layers, another optimization may be necessary. $\mathcal{C}$ serves as a valuable diagnostic that occasionally identifies hardware aberrations such as incident beam disturbances. With statistically similar maps of $\mathcal{C}$ in successive layers, an entire volume of microstructure can be reliably reconstructed.
- Simulated detector images. The codes can generate detector image files (with binary format the same as input images) based on reconstructed microstructures or arbitrary orientation inputs. Comparing these images with raw detector images is frequently informative for diagnosing reconstructions with reduced $\mathcal{C}$ and characterizing the global overlap and signals that are missed due to other phases or deformation (59).

4. APPLICATIONS

4.1. Model Validation

As noted above, a key aspect of HEDM that sets it apart from other characterization methods is its ability to acquire microstructural information in a bulk 3D sample over a series of steps in time, temperature, strain, and so forth. This opens up the possibility of using HEDM data to validate codes that simulate microstructural evolution. Turner et al. (60), for example, used a finite-element code with crystal plasticity to simulate the experiment previously reported by the same group (61). Tensile loading was performed on a sample of Ti-7Al to a stress that resulted in a slight deviation from linear elastic response. Both nf- and ff-HEDM were performed in the unloaded state, and three additional loads were recorded with far field. Recall that the latter provided the full strain tensor on a per-grain basis. By taking differences between the strain under load in each grain and the initial state, Turner et al. obtained good agreement between the simulated and measured values of strain. This good agreement represents the first step toward detailed validation of such simulations at the grain scale.

Tari et al. (62) repeated this effort but took account of the initial residual strain state by using an eigenstrain approach to instantiate the simulation, which was performed with a spectral algorithm for full-field micromechanical simulation. The micromechanical analysis of stress–strain inhomogeneities with Fourier transform (MASSIF) code is based on a Green's function solution for the partial differential equations combined with the fast Fourier transform and has been fully described elsewhere (63). The eigenstrain approach mentioned above, developed by Pokharel & Lebensohn (64), consists of converting the measured strain tensor in each grain to an eigenstrain using the Eshelby (65) approach. Each eigenstrain tensor is distributed over the grid points belonging to the associated grain and used as input to MASSIF. MASSIF computes a full-field solution in the first step before proceeding to simulate the tensile test. The results showed excellent agreement on a grain-by-grain basis that gradually deteriorated with increasing strain. The good agreement can be taken as cross-validation between the HEDM measurements and the simulation approach.

4.2. Plastic Strain

The nf-HEDM technique is sufficiently robust against peak spreading that it delivers useful reconstructions of plastically deformed metals to strains of 20%, depending on the material. Li et al. (59) demonstrated that orientations could be tracked in individual grains of pure copper subjected to tensile deformation. Plotting the reorientation trajectories showed that individual grains deviate markedly from the expectations of crystal plasticity theory (66). This finding also demonstrated that the 0.1° accuracy of orientation measurement still applies to deformed material and allows considerable detail of the internal structure of grains to be quantified in the interior of polycrystalline samples. Pokharel et al. (46) refined this analysis in a follow-up experiment on pure copper and showed that, in addition to deviations from crystal plasticity, some grains split into two or more fragments that followed different reorientation paths. Even when the measured orientation map was used to instantiate a full-field viscoplastic crystal plasticity simulation, significant deviations were found for individual grains, even though the average texture development was as expected. No correlation was found between orientation and intragranular orientation gradients. Pokharel et al. (17) later showed that misorientation increases monotonically with strain, as expected, and that it is associated with grain fragmentation, that is, a steady decrease in grain size. In particular, they pointed out a link between orientation gradients, as quantified by kernel average misorientation (KAM), and distance from microstructural features such as grain boundaries. In general, KAM decreases with distance from grain boundaries, which is reasonable given that a grain boundary represents a discontinuity in properties (both elastic and plastic), but substantial variations from one grain to another were evident. The relationship between orientation gradients and microstructural distance was investigated further by Subedi et al. (67), who found that the spatial resolution of the orientation mapping technique must be comparable to the dislocation cell size for accurate assessment, which means that caution is required with HEDM maps on a 1-μm point spacing, in comparison to the typical submicrometer cell size in most metals deformed at room temperature.

Aydıner et al. (68) used HEDM to measure the mechanical response of an individual grain in the bulk of a magnesium alloy (AZ31) that exhibited twinning. They found that the stress state in the twin was clearly different from that in the matrix. This represented an early example of the capability of ff-HEDM to quantify individual transformation-like events in the bulk. Lind et al. (12) reported a tensile test on pure zirconium in which mechanical twins were detected in the bulk of the sample. The 3D orientation map of the initial, undeformed microstructure allowed the full elastic stress field to be calculated in addition to the Schmid factors for each potential twin system.

Although some twins formed at high Schmid factor, remarkably, several formed with negative values. Moreover, use of the local stress based on the full-field simulation that takes account of the significant elastic anisotropy in zirconium modified the (local) Schmid factors but did not change the conclusions. These results are hard to explain unless the local slip activity influences, say, the nucleation of mechanical twins. This scenario is illustrated in **Figure 12*a***, which shows a small area around a twinned grain. **Figure 12*b*** and ***c*** show prismatic slip events identified by characteristic lattice rotations about the crystalline *c* axis. Both the twinning and slip observations were observed in adjacent layers, yielding fully 3D observations. Abdolvand et al. (69) performed a similar experiment in coarse-grained Zircaloy-2 and measured substantial increases in the number of grains thanks to mechanical twinning. In grains with high Schmid factors for twinning based on the global average stress, most of the six variants were observed. Although the variant with the highest Schmid factor was always dominant, the availability of the local strain in each grain enabled calculation of a local Schmid factor for each variant. In all grains, including those less favorably oriented for twinning, the local Schmid factor explained the occurrence of what would otherwise have been highly unlikely twins, which was interpreted as being caused by slip (and twinning) in neighboring grains.

Pagan et al. (71, 72) used ff-HEDM to measure elastic strains on a per-grain basis roughly every 0.03% strain in a tensile test of polycrystalline Ti-7Al strained to 2.5%. The elastic strain in each grain is readily transformed to stress by use of anisotropic elasticity. The stress can then be projected onto each slip system, of which there are four in this hexagonal alloy: basal, prismatic, pyramidal $\langle a \rangle$, and pyramidal $\langle c + a \rangle$ as a resolved shear stress (RSS). The median of the maximum RSS values was interpreted as the critical RSS for the systems, which showed strongly different behaviors on the different slip systems: The basal and prismatic exhibited a peak around the yield point, whereas the pyramidal $\langle c + a \rangle$ exhibited steady hardening. Thus, the behavior of each separate system was clearly different from that of the polycrystal as a whole, which exhibited a nearly perfect elastic–perfectly plastic response. A repeat of this analysis at elevated temperature (72) showed similar behavior, except that there was minimal softening on the basal, prismatic, and pyramidal $\langle a \rangle$ systems with monotonic hardening on the pyramidal $\langle c + a \rangle$ system at a lower rate compared with room temperature. Overall, these experiments demonstrate the ability of HEDM to provide far more detailed information about slip behavior than traditional experiments. This point is particularly important because grains embedded in polycrystals are known to behave differently from isolated single crystals. Many other aspects of plasticity at the slip system level are potentially accessible via HEDM. Tayon et al. (73) showed that softening in AlLi could be linked to grain orientation.

Regarding the more specialized approach of examining individual peaks in the very far field, Pagan et al. (74) examined shear bands during compression of a single copper crystal. In this case, knowledge of the crystal orientation enabled the authors to steer the detectors to capture individual diffracted beams, which were then used to generate single-crystal orientation pole figures (SCPFs) (33, 34). The changes in these SCPFs were linked via simulation to the predominant active slip system in each shear band, which showed that the macroscopic geometry of the shear band does not correspond closely to the slip plane and direction. Chatterjee et al. (75) used a special high-speed detector, also in the very far field, in conjunction with ff-HEDM for mapping the polycrystal structure to monitor individual diffraction spots in samples of Ti-7Al and the magnesium alloy AZ31. They found numerous examples of jumps in elastic strain associated with step changes in spot position and shape in the very far field, which they interpreted as evidence for intermittency, that is, bursts in plastic strain. Earlier, Beaudoin et al. (76) monitored elastic strains in a titanium alloy under creep conditions by using an HEDM-related technique and found evidence for avalanche behavior, that is, bursts of dislocation activity under steady loading.

4.3. Fatigue Studies

Fatigue is an extensively studied problem that nevertheless presents numerous puzzles at the microstructural scale. Spear et al. (13) studied crack surfaces in a tension–tension fatigue fractured sample of aluminum 6061 alloy. The cyclic loading was varied so as to imprint marker bands on the fracture surfaces at regular intervals, allowing the crack growth front to be traced out around the initiation point. The aim was to combine CT with HEDM to measure the grain orientations on either side of the crack surface. The authors cut the characterized sample from the full specimen so as to include the crack origination point and be able to study the early stages of growth. The CT-HEDM combination enabled each local facet of the fracture surface to be indexed, which showed that 100 and 110 surface normals predominated, with 111 being the least common; the initiation point itself had a normal close to 100. The local propagation rate varied significantly as the crack progressed. As Herbig et al. (77) observed previously for a similar experiment on body-centered cubic titanium alloy 21S (which used a different diffraction microscopy technique), the rules that govern crack propagation at the microstructural scale remain unclear, despite the richly detailed data.

Modeling by Cerrone et al. (78) exemplifies a different use of HEDM data for the study of fatigue. This study was based on HEDM measurement of a sample of René88DT. The cyclic loading was interrupted from time to time so that the replica technique could be used to check for the presence of cracks at the scale of individual grains, and the test was stopped once there was a definite indication of at least one microcrack. A smaller sample that contained the known microcrack was taken and used for HEDM characterization. Cerrone et al. used the resulting data to construct a volume element, run finite-element simulations with crystal plasticity, and investigate why the microcrack occurred in the particular observed location along a coherent twin boundary. The results demonstrate the importance of elastic anisotropy that gives rise to high RSSs on slip systems that are coplanar with the boundary. Since such coherent twin boundaries often span a grain, large grains allow slip to accumulate, leading to crack formation, as also discussed by Stein et al. (79). Naragani et al. (80) used a combination of HE-μCT and ff-HEDM to study cyclic deformation of a nickel-based superalloy sample that was seeded with a nonmetallic inclusion large enough to be visible in the tomography. The tomography revealed the initiation and propagation of a fatigue crack from the inclusion, and HEDM showed that strain heterogeneity developed within a few cycles and was then largely stable. The measurements were complemented by use of elasto-viscoplastic full-field simulations based on Fourier transforms. The combined approach enabled the development of a model of crack initiation from the particle. Recently, Murphy-Leonard et al. (81) used HEDM to show that tension–compression asymmetry during cyclic loading in Mg is linked to twinning–detwinning events.

4.4. Annealing

An early study of annealing with nf-HEDM by Hefferan et al. (15) showed both sharpening of diffraction peaks, consistent with recovery processes, and the appearance of new orientations, as expected for recrystallization. Lin et al. (82) revisited an old question of whether annealing twins can form via the decomposition of grain boundaries. This mechanism had been inferred from surface observations by, for instance, Fullman & Fisher (83), who noted that certain grain boundaries adjacent to triple lines appeared to split into two new boundaries of which one was a coherent twin boundary, that is, a $\Sigma 3$ with 111 boundary planes; this boundary is the lowest energy in any face-centered cubic metal by a substantial margin (e.g., 84). By analyzing successive HEDM images from a grain growth experiment in pure nickel that was originally undertaken by Hefferan et al. (85), Lin et al. (82) showed that new grains appeared at triple lines during grain growth and that

they invariably included a twin relationship between the new grain and the grain within which it appeared. Measurement of dihedral angles provided evidence that the net change in grain boundary energy was a decrease, as required for the spontaneous appearance of a new grain, thereby confirming the decades-old surface observations (83).

Three recent nf-HEDM measurements (86–88) have found that classical ideas such as the initial size of an individual grain and its number of neighbors are poor predictors of growth. Instead, the number of faces of a given grain minus the average face number of its neighbors (the excess face number) turns out to be a much better predictor of behavior in grain growth; however, the distribution of responses of sets of grains with the same excess face number is broad, so this parameter is not predictive of an individual grain's behavior. These studies sampled large ensembles of grains (in the thousands) and tracked their evolution in three dimensions over successive annealing treatments. These findings demonstrate the importance of grain neighborhood, which confirms some long-standing suppositions in grain growth modeling (e.g., 89).

4.5. Shape Memory Alloys

The Stebner group (90–92) has applied HEDM to shape memory alloys. Bucsek et al. (90) presented a forward modeling approach for resolving the advent of martensitic phases on the basis of HEDM data. The same group studied the grain refinement of a single crystal of NiTi subjected to thermal cycling that caused phase transformation between the high-temperature austenite and low-temperature martensitic phases (91). The authors noted that $\Sigma 3$ and $\Sigma 9$ grain boundaries formed during the grain refinement. Under deformation, such alloys respond in a complex fashion, exhibiting macroscale deformation bands with nucleation and growth of multiple twin variants of martensite at the microscale. Again, multiple synchrotron X-ray diffraction techniques, including HEDM, were brought to bear on the problem (92).

4.6. Shock Loading and Void Formation

Density-based tomography is perhaps the oldest form of 3D microscopy. The high-intensity parallel beams available at synchrotrons are well suited to this task, provided that the sample is small enough to fit within the 2–3-mm width that is typically available. Reconstruction can be performed with standard algorithms such as back projection and Fourier transforms, as found in, for instance, TomoPy (93). CT is practiced at both the micrometer and nanometer scales; the optics are simple in the former case and more complex in the latter (94). Combining HEDM with HE-μCT has proven useful for the analysis of voids in relation to microstructure. Menasche et al. (14) performed nf-HEDM on a sample of pure copper that was then subjected to shock (i.e., dynamic) loading to the point of incipient damage that was sufficient to form isolated voids but not to fracture the sample. Upon recovery of the sample, a second round of HEDM combined with HE-μCT revealed several hundred voids. By compensating for the plastic strain, the voids were registered with respect to the original microstructure, which showed that most of them were located along grain boundary triple lines. This result demonstrates that 3D characterization is necessary for this type of problem. A further analysis revealed the unexpected result that no special crystallographic character distinguished the grain boundaries that were in contact with the voids. Specifically, there was no evidence that $\Sigma 3$ boundaries favored or disfavored void formation despite the low energy of coherent twin boundaries, that is, $\Sigma 3$ with 111 boundary plane. Lieberman et al. (95) extended this experimental analysis by using the undeformed structure to instantiate an elasto-viscoplastic micromechanical simulation using an image-based method. The many theories for void formation include the reasonable idea that traction across a grain boundary plane (i.e., parallel to the normal) should be a primary cause of decohesion. The finding that the only strong correlation was with

the plastic activity was therefore unexpected. In other words, voids were most likely to be present when there was a strong difference in Taylor factor or slip activity across a grain boundary. Once again, the capacity of HEDM to measure microstructure in advance of loading a sample was essential for advancing understanding of a physical phenomenon. This research has been followed up by a number of modeling-based studies that seek to interpret the results (96, 97), as well as combinations of tomography and electron microscopy (98, 99). A similar application to thermally induced voids (100) has also been performed.

4.7. Irradiation

Zhang et al. (101) used ff-HEDM to compare grain characteristics of a neutron-irradiated (450°C, 0.01 dpa) Fe-9Cr specimen and its unirradiated counterpart, both prior to and after plastic tensile deformation. For the undeformed specimens, they found that neutron irradiation had no effect on the grain sizes but that it increased the intragranular strain distribution. After deformation, grains fragmented into subgrains in both unirradiated and irradiated specimens: The irradiated specimen contained a few large subgrains that coexisted with many smaller subgrains, while the unirradiated specimen contained small subgrains with a relatively uniform size distribution. These first-of-a-kind grain-scale measurements provided new insight into the effects of neutron irradiation on the mechanical response of these FeCr structural alloys.

4.8. Functional and Geological Materials

In addition to the various applications to metals and ceramics described briefly above, HEDM has found use in functional and geological materials. Daniels et al. (102) used ff-HEDM to investigate elastic strains in a polycrystalline sample of $BaTiO_3$ that had been transformed from cubic to rhombohedral via the application of an electric field. Although there was an average relationship between grain orientation and response to the field, the local strain in each grain indicated that there were also significant deviations from that average behavior. Daniels et al. determined that average behavior appears for grain clusters of order 20 grains. As with other materials, the local environment of any given grain has a strong influence on its response to far-field loading. The high-pressure materials community has recently recognized the potential for ff-HEDM for analyzing micrometer-scale samples at pressures above 1 Mbar. Generally speaking, in cases where the material phase of interest is synthesized in a diamond anvil cell at high pressure and/or temperature it is difficult to obtain a powder sample suitable for traditional structural refinement. Both grain growth and recrystallization conspire to coarsen the grain size in the sample chamber, which yields the spotty diffraction patterns suitable for ff-HEDM. Zhang et al. (103) demonstrated the feasibility of applying ff-HEDM to the in situ single-crystal structure determination of $(Mg,Fe)SiO_3$ postperovskite—the main mineral in the D'' layer in Earth's mantle—at high pressure in a diamond anvil cell. Since that study, ever more sophisticated applications of ff-HEDM have been applied to diamond anvil cell experiments. Nisr et al. (35) applied in situ ff-HEDM at 90 GPa coupled with line profile analysis to investigate dislocation behavior in $MgGeO_3$ postperovskite [a lower-pressure analog to $(Mg,Fe)SiO_3$]. Their main result was to identify (001) as the dominant slip plane, which was consistent with information on seismic activity in the D'' layer. The nf-HEDM technique could be applied to diamond anvil cell studies in the future, pending the development of specialized scintillators.

4.9. Thermal Expansion

As an example of a new application of the method, the Lim group has conducted experiments to measure the coefficient of thermal expansion (CTE) in Ti-7Al (R.E. Lim, D.C. Pagan, D.E.

Boyce & A.D. Rollett, manuscript in preparation). The anisotropy in thermal expansion between the *a* and *c* axes results in significant variations in elastic strain at the grain scale, even after the overall expansion is subtracted out. Moreover, the magnitude of the internal stresses varies over the range of temperature used in the measurement. The main result is a variation in the ratio of the CTE values on either side of unity, which helps explain inconsistent reports in the literature. This result, combined with the grain growth examples discussed above, illustrates the value of extending HEDM experiments to high temperatures.

5. DISCUSSION

5.1. Distinctive Characteristics of High-Energy Diffraction Microscopy

HEDM combines several characteristics that make it highly distinctive, if not actually unique, namely (*a*) its nondestructive nature, which allows repeated measurements between and during loading of the sample, (*b*) its high crystallographic orientation accuracy, which allows, for instance, mapping of subgrain networks, (*c*) its ability (in the near-field variant) to map on a regular grid, and (*d*) its ability to measure the complete strain tensor, in contrast to surface probes such as EBSD. There is a trade-off between these useful characteristics and the cost of human effort to reconstruct the 3D microstructures from voluminous raw data and the competitive nature of gaining access to beam time. Therefore, this technique is expected to be used for problems involving evolution in time, such as grain growth (104), or in strain (62). It has also been used for the development of crystal plasticity models (105, 106) because the strain tensor is readily converted to a stress tensor that can, in turn, be resolved onto any particular slip system. Distributions in RSS provide information about evolution in the critical RSS on different slip systems, which provides crucial information about crystal plasticity.

5.2. Relation to Other X-Ray Methods

HEDM nondestructively probes microstructures in millimeter-sized samples with resolution from the micrometer to millimeter length scales. A number of complementary X-ray probes have been developed contemporaneously. In this section, we briefly describe these techniques and their relation to the methods described above. We provide a few citations to technique descriptions and example applications; these citations are not exhaustive. Similar techniques are being applied to the analysis of neutron scattering. Cereser et al. (107) have presented a method for reconstructing polycrystalline materials from time-of-flight neutron data that includes crystal orientation. This method will likely be useful for coarser grain sizes than are feasible with X-ray-based HEDM.

5.2.1. Diffraction contrast tomography. Diffraction contrast tomography (DCT) (42, 108–110) produces 3D grain maps using a box beam rather than the line-focused beam typical for nf-HEDM. This has the advantage of obtaining 3D information from a single rotation scan. Entire 3D maps of grain can be obtained from a single rotation scan. For example, Zhang et al. (86) used this technique to study grain growth in iron and addressed the question of how well growth of individual grains could be predicted via the MacPherson–Srolovitz theory. Notwithstanding the utility of the method, plastic strain with its peak broadening means that only very lightly deformed samples are suitable for DCT. This technique has recently been ported to laboratory-based X-ray systems and is available commercially as a modified tomography system (111, 112).

5.2.2. Differential aperture X-ray microscopy. Differential aperture X-ray microscopy (113, 114) uses a micrometer or smaller focused, broad-spectral-range beam combined with an area

detector that collects Laue diffraction patterns. 3D spatial resolution is obtained by scanning a platinum wire across the sample surface. Beam energies extend to ∼20 keV, so deep penetration in many materials (**Figure 2**) is limited. In contrast, spatial resolution is determined by the beam size, so it can be less than a micrometer. Deviatoric strain tensors can be resolved to less than 10^{-4}. With a clever design, a monochromator can be inserted so as to yield absolute strains.

5.2.3. Bragg coherent diffractive imaging. Bragg coherent diffractive imaging (BCDI) uses coherent illumination of a nanoscale crystal or grain combined with far-field detection of a Bragg peak to measure the Fourier power spectrum of the entire grain structure. Resultant density maps resolve the grain shape and the internal atomic displacement fields (relative to the crystal structure that generates the Bragg peak) with ∼30 nm resolution (115–118). Most studies are based on a single Bragg peak, thereby yielding displacements along a single direction (the direction of **Q**), but recent research (119) has used multiple peaks to obtain full 3D displacements. This technique is complementary to HEDM in that, while HEDM measures micrometer to millimeter responses in polycrystals, BCDI can view the underlying nanoscale mechanisms. Efforts are under way to apply BCDI to polycrystalline environments so as to observe dislocation motion and interactions. At the same time, progress toward resolving coherent signals using more highly penetrating high-energy X-rays are showing promise (120). Coming synchrotron upgrades will yield more highly coherent high-energy beams and will facilitate combined HEDM and BCDI measurements on materials with grain sizes up to 1 μm.

5.2.4. Dark field X-ray microscopy. Dark field X-ray microscopy is a recently developed technique that builds on extensive research in transmission electron microscopy methods. In a series of papers (28, 121–123), a group based at the Danish Technical University and ESRF developed an instrument at ESRF that focuses a diffracted beam with a compound refractive lens (CRL) onto a detector placed a few meters from the sample. The placement of the CRL at the back focal plane both provides magnification of the features of interest and selects a particular diffracted beam. The latter is helpful when working with a polycrystalline sample, which can lead to confusion arising from overlapping reflections. With the appropriate motorized stages, a rocking curve technique allows images to be obtained across the selected Bragg peak. This capability has been demonstrated (123) by imaging dislocations in a single-crystal sample of diamond: The conventional near-field image simply shows all the defects present, but dark field microscopy allows detailed mapping of the displacement fields of individual dislocations. The method is analogous to weak beam imaging in transmission electron microscopy but with significantly better strain resolution. This technique is directly related to HEDM in that the same setup (without the CRL and without requiring large-scale coherence) can be used to first map out a large microstructural region in order to allow a particular grain, with fully determined orientation and within a known neighborhood, to be interrogated at the nanoscale. Similar to BCDI, this technique uses extensive measurements to probe a single grain, yielding 1D information on atomic displacements (along the chosen **Q**).

5.2.5. Pencil beam methods. Pencil beam methods were developed originally (124) at ESRF and more recently by Hayashi et al. (125, 126) at SPring-8. In these methods, a monochromatic point-focused or pencil beam approximately 1 μm square illuminates a line through the sample. The sample is rotated, and diffraction patterns are collected from successive lines. As the sample is displaced relative to the rotation axis, voxels are illuminated at a sequence of angles of incidence. While slower than the HEDM methods described herein, pencil beam methods have the notable advantage over both ff-HEDM and nf-HEDM that, with the aid of a conical slit, the set of spots associated with each resolution-limited volume element can be indexed even in samples with

significant deformation. This means that an orientation map can be obtained that also contains the full strain tensor at each point (125), thereby revealing the substantial intragranular strain (or stress) gradients that are predicted to exist from simulations. To date, these methods have been demonstrated on a low-carbon single-phase steel sample (125–127). Again, these methods, which do not depend on large coherence lengths, will benefit from synchrotron upgrades with their increased brilliance.

5.3. Ongoing Developments

With the increasing number of HEDM applications, demand for experiment time at the APS 1-ID-E facility has reached a point at which highly rated General User Proposals are not allocated time until after a substantial (frequently 4- to 8-month) delay. In response to this situation, and with the maturity of the techniques, a new HEDM instrument is being built in the 6-ID-D hutch at the APS. The High Throughput HEDM instrument, funded by the National Science Foundation Major Research Infrastructure program (via a grant to the HT-HEDM Consortium, consisting of CMU, Colorado School of Mines, Purdue University, and University of Utah) and with beamline infrastructure provided by the APS, will use updated detector and controls technology to perform nf- and ff-HEDM and high-energy tomography measurements and will stream data to high-performance computing facilities for near-real-time reconstructions. Relatively straightforward sample environments that do not require major equipment reconfigurations will be accommodated. More complex sample environments and measurements requiring large sample-to-detector distances will remain at 1-ID-E. This instrument will also complement recent and continuing facility developments at CHESS.

In parallel with new instrument development, research continues to accelerate reconstructions and to expand and validate (44) output data sets. New Python- and GPU-based code has been developed at CMU. Output microstructures are image based, and a variety of formats are currently available (see the HEXOMAP link in **Table 1**). This code will also enable local strain state/lattice constant optimization and greatly accelerated experimental geometry parameter optimizations (H. Liu, Y.-F. Shen & R.M. Suter, manuscript in preparation). The HEXRD project is an open-source suite of diffraction tools that provides multidetector instrument support, a graphical user interface, high-precision calibration utilities, powder diffraction analysis tools, nf-HEDM orientation field reconstruction, and batch processing of ff-HEDM time-series data. HEXRD is still under active development and is currently employed at CHESS and the Advanced Light Source (ALS).

5.4. Impact of Synchrotron Upgrades for High-Energy Diffraction Microscopy

An upcoming upgrade of the APS storage ring will result in a new magnetic lattice in a multi-bend achromat configuration. This upgrade will deliver substantially increased brightness and improved transverse coherence. Along with the ring upgrade, there will be several new feature beamlines, including two exploiting coherence above 40 keV, namely the Coherent High-Energy X-Ray (CHEX) and High-Energy X-Ray Microscope (HEXM) beamlines. CHEX will have several end stations, with at least one capable of delivering a fixed high-energy X-ray beam. HEXM will be fully tunable over the 40–120 keV range (similar to 1-ID) and will have a large (20 m long) end station located outside the current hall, ~180 m from the source. This will enable the use of a wide range of beam sizes, ranging from approximately 0.4×0.2 μm to several millimeters. The large end station will enable BCDI at these high energies on up-to-micrometer-sized grains, as was recently demonstrated at 1-ID using the (partially coherent) current storage ring (120). These features will enhance the spatiotemporal resolution of both diffraction- and absorption-based imaging capabilities (discussed above) and will all be accessible within a single experiment.

6. SUMMARY AND PROSPECTS

HEDM as a method for mapping microstructure in bulk 3D polycrystals is well developed and is making contributions in many areas of materials science and the mechanics of materials. A reasonable expectation is that the analysis codes will continue to be made more robust and usable alongside acquisition so that HEDM becomes a microscopy in its own right, as opposed to a technique that requires substantial postacquisition effort to obtain 3D images and fields. Construction of new beamlines with enhanced X-ray properties and more streamlined data flows is under way, for example, at the APS. There is a need for verification of reconstructions under varied sample states and validation against ground truth, whether experimental or theoretical. Characterizing samples across different facilities is another useful activity. Methods for accelerating the analysis codes are under investigation, with GPUs offering one obvious route. Machine learning (ML) appears to be an obvious opportunity for speeding up HEDM analysis and enabling high-throughput approaches (see the remarks about upgrades in Section 5.4). Nevertheless, few examples are available. Laanait et al. (128) implemented an ML approach for BCDI data acquired on a sample of PbZr titanate; they used a combination of k-means clustering and principal component analysis to identify interesting features of the anisotropic defect structures in this material. Cherukara et al. (129) recently applied deep learning techniques to reconstruction of BCDI data, partly motivated by the desire to speed up the process and give researchers access to results during data acquisition sessions. Improvements in the technical capability of HEDM are likely to continue, with strain refinement of the near-field method as one example.

HEDM can also be combined with other techniques. The use of HEDM with nanoscale X-ray techniques is one way to survey a polycrystalline sample before zooming in to examine specific individual grains. As described above for Bragg coherent diffraction and dark field microscopy, this combined technique is currently under development.

DISCLOSURE STATEMENT

The authors are not aware of any affiliations, memberships, funding, or financial holdings that might be perceived as affecting the objectivity of this review.

ACKNOWLEDGMENTS

The writing of this review was performed partly under the auspices of the US Department of Energy (DOE) by Lawrence Livermore National Laboratory under contract DE-AC52-07NA27344 (LLNL-JRNL-806858). Support at Carnegie Mellon University for the development of this review includes grants from the Air Force Office of Scientific Research (FA9550-16-1-0105), DOE/Basic Energy Sciences (DESC0019096), DOE/National Nuclear Security Administration (DE-NA0003915), and the National Science Foundation "Designing Materials to Revolutionize and Engineer our Future" program (DMR-1628994). Work at the Advanced Photon Source, an Office of Science User Facility operated for the DOE Office of Science by Argonne National Laboratory, was supported by the DOE under contract DE-AC02-06CH11357. The authors are grateful for discussions about HEDM with Ulrich Lienert, Darren Pagan, Paul Shade, Peter Kenesei, Hemant Sharma, Jun-Sang Park, and the many postdocs and students we have worked with.

LITERATURE CITED

1. Sorby H. 1864. *On a new method of illustrating the structure of various kinds of "blister" steel by nature printing*. Paper presented at Sheffield Literary and Philosophical Society, Febr.

2. Uchic MD, Groeber MA, Dimiduk DM, Simmons JP. 2006. 3D microstructural characterization of nickel superalloys via serial-sectioning using a dual beam FIB-SEM. *Scr. Mater.* 55:23–28
3. Schwartz A, Kumar M, Adams B. 2000. *Electron Backscatter Diffraction in Materials Science*. New York: Kluwer
4. Douglas JE, Echlin MP, Lenthe WC, Seshadri R, Pollock TM. 2015. Three-dimensional multimodal imaging and analysis of biphasic microstructure in a Ti–Ni–Sn thermoelectric material. *APL Mater.* 3:096107
5. Poulsen HF. 2004. *Three-Dimensional X-Ray Diffraction Microscopy*. Springer Tracts Mod. Phys. 205. Berlin: Springer
6. Lauridsen E, Schmidt S, Suter R, Poulsen HF. 2001. Tracking: a method for structural characterization of grains in powders or polycrystals. *J. Appl. Crystallogr.* 34:744–50
7. Poulsen HF, Nielsen S, Lauridsen E, Schmidt S, Suter R, et al. 2001. Three-dimensional maps of grain boundaries and the stress state of individual grains. *J. Appl. Crystallogr.* 34:751–56
8. Poulsen HF, Vaughan GBM. 2019. Multi-grain crystallography and three-dimensional grain mapping. In *International Tables for Crystallography: Powder Diffraction*, Vol. H, ed. CJ Gilmore, JA Kaduk, H Schenk, pp. 606–16. New York: Wiley
9. Pokharel R. 2018. Overview of high-energy X-ray diffraction microscopy (HEDM) for mesoscale material characterization in three dimensions. In *Materials Discovery and Design*, ed. T Lookman, S Eidenbenz, F Alexander, C Barnes, pp. 167–201. Cham, Switz.: Springer
10. Li S, Suter R. 2013. Adaptive reconstruction method for three-dimensional orientation imaging. *J. Appl. Crystallogr.* 46:512–24
11. Suter R, Hennessy D, Xiao C, Lienert U. 2006a. Forward modeling method for microstructure reconstruction using X-ray diffraction microscopy: single crystal verification. *Rev. Sci. Instrum.* 77:123905
12. Lind J, Li S, Pokharel R, Lienert U, Rollett A, Suter R. 2014. Tensile twin nucleation events coupled to neighboring slip observed in three dimensions. *Acta Mater.* 76:213–20
13. Spear AD, Li SF, Lind JF, Suter RM, Ingraffea AR. 2014. Three-dimensional characterization of microstructurally small fatigue-crack evolution using quantitative fractography combined with postmortem X-ray tomography and high-energy X-ray diffraction microscopy. *Acta Mater.* 76:413–24
14. Menasche D, Lind J, Li S, Kenesei P, Bingert J, et al. 2016. Shock induced damage in copper: a before and after, three-dimensional study. *J. Appl. Phys.* 119:154902
15. Hefferan C, Li S, Lind J, Lienert U, Rollett A, Suter R. 2012. Observation of recovery and recrystallization in high purity aluminum measured with forward modeling analysis of high energy diffraction microscopy. *Acta Mater.* 60:4311–18
16. Pokharel R, Brown D, Clausen B, Byler D, Ickes T, et al. 2017. Non-destructive characterization of UO_{2+x} nuclear fuels. *Microsc. Today* 25:42–47
17. Pokharel R, Lind J, Li S, Kenesei P, Lebensohn R, et al. 2015. In situ observation of bulk 3D grain evolution during plastic deformation in polycrystalline copper. *Int. J. Plast.* 67:217–2343
18. Schuren J, Shade P, Bernier J, Li S, Blank B, et al. 2015. New opportunities for quantitative tracking of polycrystal responses in three dimensions. *Curr. Opin. Solid State Mater. Sci.* 19:235–44
19. Kittel C. 2005. *Introduction to Solid State Physics*. New York: Wiley. 8th ed.
20. Als-Nielsen J, McMorrow D. 2011. *Elements of Modern X-Ray Physics*. New York: Wiley. 2nd ed.
21. Shastri S, Fezzaa K, Mashayekhi A, Lee WK, Fernandez P, Lee P. 2002. Cryogenically cooled bent double-Laue monochromator for high-energy undulator X-rays (50–200 keV). *J. Synchrotron Radiat.* 9:317–22
22. Shastri SD. 2004. Combining flat crystals, bent crystals and compound refractive lenses for high-energy X-ray optics. *J. Synchrotron Radiat.* 11:150–56
23. Shastri SD, Almer J, Ribbing C, Cederström B. 2007. High-energy X-ray optics with silicon saw-tooth refractive lenses. *J. Synchrotron Radiat.* 14:204–11
24. Lienert U, Li S, Hefferan C, Lind J, Suter R, et al. 2011. High-energy diffraction microscopy at the advanced photon source. *J. Miner.* 63:70–77
25. Cullity BD. 1956. *Elements of X-Ray Diffraction*. Reading, MA: Addison-Wesley

26. Lee JH, Aydıner CC, Almer J, Bernier J, Chapman KW, et al. 2008. Synchrotron applications of an amorphous silicon flat-panel detector. *J. Synchrotron Radiat.* 15:477–88
27. Lee J, Almer J, Aydner C, Bernier J, Chapman K, et al. 2007. Characterization and application of a Ge amorphous silicon flat panel detector in a synchrotron light source. *Nucl. Instrum. Methods A* 582:182–84
28. Poulsen HF, Cook PK, Leemreize H, Pedersen AF, Yildirim C, et al. 2018. Reciprocal space mapping and strain scanning using X-ray diffraction microscopy. *J. Appl. Crystallogr.* 51:1428–36
29. Schuren JC, Shade PA, Bernier JV, Li SF, Blank B, et al. 2015. New opportunities for quantitative tracking of polycrystal responses in three dimensions. *Curr. Opin. Solid State Mater. Sci.* 19:235–44
30. Poulsen HF. 2012. An introduction to three-dimensional X-ray diffraction microscopy. *J. Appl. Crystallogr.* 45:1084–97
31. Hansen PC, Sørensen HO, Sükösd Z, Poulsen HF. 2009. Reconstruction of single-grain orientation distribution functions for crystalline materials. *SIAM J. Imaging Sci.* 2:593–613
32. Barton NR, Bernier JV. 2012. A method for intragranular orientation and lattice strain distribution determination. *J. Appl. Crystallogr.* 45:1145–55
33. Pagan DC, Miller MP. 2014. Connecting heterogeneous single slip to diffraction peak evolution in high-energy monochromatic X-ray experiments. *J. Appl. Crystallogr.* 47:887–98
34. Pagan DC, Miller MP. 2016. Determining heterogeneous slip activity on multiple slip systems from single crystal orientation pole figures. *Acta Mater.* 116:200–11
35. Nisr C, Ribàrik G, Ungàr T, Vaughan GBM, Cordier P, Merkel S. 2012. High resolution three-dimensional X-ray diffraction study of dislocations in grains of $MgGeO_3$ postperovskite at 90 GPa. *J. Geophys. Res. Solid Earth* 117:B03201
36. Bernier J, Barton N, Lienert U, Miller M. 2011. Far-field high-energy diffraction microscopy: a tool for intergranular orientation and strain analysis. *J. Strain Anal. Eng. Des.* 46:527–47
37. Jakobsen B, Poulsen HF, Lienert U, Almer J, Shastri SD, et al. 2006. Formation and subdivision of deformation structures during plastic deformation. *Science* 312:889–92
38. Jakobsen B, Poulsen HF, Lienert U, Pantleon W. 2007. Direct determination of elastic strains and dislocation densities in individual subgrains in deformation structures. *Acta Mater.* 55:3421–30
39. Lienert U, Almer J, Jakobsen B, Pantleon W, Poulsen HF, et al. 2008. Single grain characterization techniques at the APS 1-ID beamline. In *Final Program of the 137th TMS Annual Meeting and Exhibition: Linking Science and Technology for Global Solutions*, p. 287. Pittsburgh, PA: TMS
40. Pantleon W, Wejdemann C, Jakobsen B, Lienert U, Poulsen HF. 2009. Evolution of deformation structures under varying loading conditions followed in situ by high angular resolution 3DXRD. *Mater. Sci. Eng. A* 524:55–63
41. Lienert U, Ribárik G, Ungar T, Wejdemann C, Pantleon W. 2017. High-resolution single-grain diffraction of polycrystalline materials. *Synchrotron Radiat. News* 30:35–40
42. Ludwig W, Reischig P, King A, Herbig M, Lauridsen E, et al. 2009. Three-dimensional grain mapping by X-ray diffraction contrast tomography and the use of Friedel pairs in diffraction data analysis. *Rev. Sci. Instrum.* 80:033905
43. Suter R, Hennessy D, Xiao C, Lienert U. 2006. Forward modeling method for microstructure reconstruction using X-ray diffraction microscopy: single-crystal verification. *Rev. Sci. Instrum.* 77:123905
44. Menasche DB, Shade PA, Suter RM. 2020. Accuracy and precision of near-field HEDM forward-model based microstructure reconstructions. *J. Appl. Crystallogr.* 53:107–16
45. Lind J, Rollett A, Pokharel R, Hefferan C, Li S, et al. 2014. Image processing in experiments on, and simulations of, plastic deformation of polycrystals. In *Proceedings of the IEEE International Conference on Image Processing*, pp. 4877–81. Piscataway, NJ: IEEE
46. Pokharel R, Lind J, Kanjarla A, Lebensohn R, Li S, et al. 2014. Polycrystal plasticity: comparison between grain-scale observations of deformation and simulations. *Annu. Rev. Condens. Matter Phys.* 5:317–46
47. Ivanyushenkov Y, Harkay K, Borland M, Dejus R, Dooling J, et al. 2017. Development and operating experience of a 1.1-m-long superconducting undulator at the advanced photon source. *Phys. Rev. Accel. Beams* 20:100701

48. Shade P, Menasche D, Bernier J, Kenesei P, Park JS, et al. 2016. Fiducial marker application method for in situ multimodal X-ray experiments. *J. Appl. Crystallogr.* 49:700–4
49. Hommer GM, Park JS, Collins PC, Pilchak AL, Stebner AP. 2017. A new in situ planar biaxial far-field high energy diffraction microscopy experiment. In *Advancement of Optical Methods in Experimental Mechanics*, Vol. 3, ed. S Yoshida, L Lamberti, C Sciammarella, pp. 61–70. Berlin: Springer
50. Park JS, Horn C, Ramanathan P, Kenesei P, Veseli S. 2019. Data management and processing workflow for the materials physics and engineering group beamlines at the advanced photon source. *J. Synchrotron Radiat.* 26:373–381
51. Schwarz N, Veseli S, Jarosz D. 2019. Data management at the advanced photon source. *Synchrotron Radiat. News* 32:13–18
52. Arkilic A, Allan DB, Caswell T, Li L, Lauer K, Abeykoon S. 2017. Towards integrated facility-wide data acquisition and analysis at NSLS. II. *Synchrotron Radiat. News* 30:44–45
53. Oddershede J, Schmidt S, Poulsen HF, Sørensen HO, Wright J, Reimers W. 2010. Determining grain resolved stresses in polycrystalline materials using three-dimensional X-ray diffraction. *J. Appl. Crystallogr.* 43:539–49
54. Wejdemann C, Poulsen HF. 2016. Multigrain indexing of unknown multiphase materials. *J. Appl. Crystallogr.* 49:616–21
55. Bernier JV, Miller MP, Boyce DE. 2006. A novel optimization-based pole-figure inversion method: comparison with WIMV and maximum entropy methods. *J. Appl. Crystallogr.* 39:697–713
56. Sharma H, Huizenga RM, Offerman SE. 2012. A fast methodology to determine the characteristics of thousands of grains using three-dimensional X-ray diffraction. I. Overlapping diffraction peaks and parameters of the experimental setup. *J. Appl. Crystallogr.* 45:693–704
57. Sharma H, Huizenga RM, Offerman SE. 2012. A fast methodology to determine the characteristics of thousands of grains using three-dimensional X-ray diffraction. II. Volume, centre-of-mass position, crystallographic orientation and strain state of grains. *J. Appl. Crystallogr.* 45:705–18
58. Schmidt S. 2014. *GrainSpotter*: a fast and robust polycrystalline indexing algorithm. *J. Appl. Crystallogr.* 47:276–84
59. Li S, Lind J, Hefferan C, Pokharel R, Lienert U, et al. 2012. Three dimensional plastic response in polycrystalline copper via near-field high energy X-ray diffraction microscopy. *J. Appl. Crystallogr.* 45:1098–108
60. Turner TJ, Shade PA, Bernier JV, Li SF, Schuren JC, et al. 2017. Crystal plasticity model validation using combined high-energy diffraction microscopy data for a Ti-7Al specimen. *Metall. Mater. Trans. A* 48:627–47
61. Turner TJ, Shade PA, Bernier JV, Li SF, Schuren JC, et al. 2016. Combined near- and far-field high-energy diffraction microscopy dataset for Ti-7Al tensile specimen elastically loaded in situ. *Integr. Mater. Manuf. Innov.* 5:94–102
62. Tari V, Lebensohn RA, Pokharel R, Turner TJ, Shade PA, et al. 2018. Validation of micro-mechanical FFT-based simulations using high energy diffraction microscopy on Ti-7Al. *Acta Mater.* 154:273–83
63. Lebensohn R, Kanjarla A, Eisenlohr P. 2012. An elasto-viscoplastic formulation based on fast Fourier transforms for the prediction of micromechanical fields in polycrystalline materials. *Int. J. Plast.* 32-33:59–69
64. Pokharel R, Lebensohn RA. 2017. Instantiation of crystal plasticity simulations for micromechanical modelling with direct input from microstructural data collected at light sources. *Scr. Mater.* 132:73–77
65. Eshelby JD. 1957. The determination of the elastic field of an ellipsoidal inclusion and related problems. *Proc. R. Soc. A* 241:376–96
66. Hosford W. 1993. *The Mechanics of Crystals and Textured Polycrystals*. New York: Oxford Univ. Press
67. Subedi S, Pokharel R, Rollett AD. 2015. Orientation gradients in relation to grain boundaries at varying strain level and spatial resolution. *Mater. Sci. Eng. A* 638:348–56
68. Aydıner CC, Bernier JV, Clausen B, Lienert U, Tomé CN, Brown DW. 2009. Evolution of stress in individual grains and twins in a magnesium alloy aggregate. *Phys. Rev. B* 80:024113

69. Abdolvand H, Majkut M, Oddershede J, Wright JP, Daymond MR. 2015. Study of 3-D stress development in parent and twin pairs of a hexagonal close-packed polycrystal. Part I. In-situ three-dimensional synchrotron X-ray diffraction measurement. *Acta Mater.* 93:246–55
70. Lind J. 2013. *In-situ high-energy diffraction microscopy study of zirconium under uni-axial tensile deformation*. PhD Thesis, Carnegie Mellon Univ., Pittsburgh, PA
71. Pagan DC, Shade PA, Barton NR, Park JS, Kenesei P, et al. 2017. Modeling slip system strength evolution in Ti-7Al informed by in-situ grain stress measurements. *Acta Mater.* 128:406–17
72. Pagan DC, Bernier JV, Dale D, Ko JP, Turner TJ, et al. 2018. Measuring Ti-7Al slip system strengths at elevated temperature using high-energy X-ray diffraction. *Scr. Mater.* 142:96–100
73. Tayon WA, Nygren KE, Crooks RE, Pagan DC. 2019. In-situ study of planar slip in a commercial aluminum–lithium alloy using high energy X-ray diffraction microscopy. *Acta Mater.* 173:231–41
74. Pagan DC, Obstalecki M, Park JS, Miller MP. 2018. Analyzing shear band formation with high resolution X-ray diffraction. *Acta Mater.* 147:133–48
75. Chatterjee K, Beaudoin AJ, Pagan DC, Shade PA, Philipp HT, et al. 2019. Intermittent plasticity in individual grains: a study using high energy X-ray diffraction. *Struct. Dyn.* 6:014501
76. Beaudoin AJ, Shade PA, Schuren JC, Turner TJ, Woodward C, et al. 2017. Bright X-rays reveal shifting deformation states and effects of the microstructure on the plastic deformation of crystalline materials. *Phys. Rev. B* 96:174116
77. Herbig M, King A, Reischig P, Proudhon H, Lauridsen EM, et al. 2011. 3-D growth of a short fatigue crack within a polycrystalline microstructure studied using combined diffraction and phase-contrast X-ray tomography. *Acta Mater.* 59:590–601
78. Cerrone A, Stein C, Pokharel R, Hefferan C, Lind J, et al. 2015. Implementation and verification of a microstructure-based capability for modeling microcrack nucleation in LSHR at room temperature. *Model. Simul. Mater. Sci. Eng.* 23:035006
79. Stein CA, Cerrone A, Ozturk T, Lee S, Kenesei P, et al. 2014. Fatigue crack initiation, slip localization and twin boundaries in a nickel-based superalloy. *Curr. Opin. Solid State Mater. Sci.* 18:244–52
80. Naragani D, Sangid MD, Shade PA, Schuren JC, Sharma H, et al. 2017. Investigation of fatigue crack initiation from a non-metallic inclusion via high energy X-ray diffraction microscopy. *Acta Mater.* 137:71–84
81. Murphy-Leonard AD, Pagan DC, Beaudoin A, Miller MP, Allison JE. 2019. Quantification of cyclic twinning–detwinning behavior during low-cycle fatigue of pure magnesium using high energy X-ray diffraction. *Int. J. Fatigue* 125:314–23
82. Lin B, Jin Y, Hefferan C, Li S, Lind J, et al. 2015. Observation of annealing twin nucleation at triple lines in nickel during grain growth. *Acta Mater.* 99:63–68
83. Fullman R, Fisher J. 1951. Formation of annealing twins during grain growth. *J. Appl. Phys.* 22:1350–55
84. Holm EA, Rohrer GS, Foiles SM, Rollett AD, Miller HM, Olmsted DL. 2011. Validating computed grain boundary energies in fcc metals using the grain boundary character distribution. *Acta Mater.* 59:5250–56
85. Hefferan C, Li S, Lind J, Lienert U, Rollet A, et al. 2009. Statistics of high purity nickel microstructure from high energy X-ray diffraction microscopy. *Comput. Mater. Contin.* 14:209–19
86. Zhang J, Zhang Y, Ludwig W, Rowenhorst D, Voorhees P, Poulsen H. 2018. Three-dimensional grain growth in pure iron. Part I. Statistics on the grain level. *Acta Mater.* 156:76–85
87. Bhattacharya A, Shen YF, Hefferan C, Li S, Lind J, et al. 2019. Three-dimensional observations of grain volume changes during annealing of polycrystalline nickel. *Acta Mater.* 167:40–50
88. Shen YF, Maddali S, Menasche D, Bhattacharya A, Rohrer G, Suter R. 2019. The importance of outliers: a three dimensional study of grain growth in α-phase iron. *Phys. Rev. Mater.* 3:063611
89. Marthinsen K, Hunderi O, Ryum N. 1996. The influence of spatial grain size correlation and topology on normal grain growth in two dimensions. *Acta Mater.* 44:1681–89
90. Bucsek AN, Dale D, Ko JYP, Chumlyakov Y, Stebner AP. 2018. Measuring stress-induced martensite microstructures using far-field high-energy diffraction microscopy. *Acta Crystallogr. A* 74:425–46

91. Bucsek A, Casalena L, Pagan D, Paul P, Chumlyakov Y, et al. 2019. Three-dimensional in situ characterization of phase transformation induced austenite grain refinement in nickel-titanium. *Scr. Mater.* 162:361–66
92. Bucsek AN, Pagan DC, Casalena L, Chumlyakov Y, Mills MJ, Stebner AP. 2019. Ferroelastic twin reorientation mechanisms in shape memory alloys elucidated with 3D X-ray microscopy. *J. Mech. Phys. Solids* 124:897–928
93. Gürsoy D, De Carlo F, Xiao X, Jacobsen C. 2014. TomoPy: a framework for the analysis of synchrotron tomographic data. *J. Synchrotron Radiat.* 21:1188–93
94. Liu Y, Meirer F, Williams PA, Wang J, Andrews JC, Pianetta P. 2012. *TXM-Wizard*: a program for advanced data collection and evaluation in full-field transmission X-ray microscopy. *J. Synchrotron Radiat.* 19:281–87
95. Lieberman EJ, Lebensohn RA, Menasche DB, Bronkhorst CA, Rollett AD. 2016. Microstructural effects on damage evolution in shocked copper polycrystals. *Acta Mater.* 116:270–80
96. Chandra S, Samal MK, Chavan VM, Raghunathan S. 2018. Void growth in single crystal copper—an atomistic modeling and statistical analysis study. *Philos. Mag.* 98:577–604
97. Nguyen T, Luscher D, Wilkerson J. 2019. The role of elastic and plastic anisotropy in intergranular spall failure. *Acta Mater.* 168:1–12
98. Brown AD, Pham Q, Fortin EV, Peralta P, Patterson BM, et al. 2017. Correlations among void shape distributions, dynamic damage mode, and loading kinetics. *J. Miner.* 69:198–206
99. Hong C, Fæster S, Hansen N, Huang X, Barabash RI. 2017. Non-spherical voids and lattice reorientation patterning in a shock-loaded Al single crystal. *Acta Mater.* 134:16–30
100. Menasche DB, Shade P, Lind J, LI S, Bernier J, et al. 2016. Correlation of thermally induced pores with microstructural features using high energy X-rays. *Metall. Mater. Trans. A* 47:5580–88
101. Zhang X, Li M, Park JS, Kenesei P, Sharma H, Almer J. 2018. High-energy X-ray diffraction microscopy study of deformation microstructures in neutron-irradiated polycrystalline Fe-9%Cr. *J. Nucl. Mater.* 508:556–66
102. Daniels JE, Majkut M, Cao Q, Schmidt S, Wright J, et al. 2016. Heterogeneous grain-scale response in ferroic polycrystals under electric field. *Sci. Rep.* 6:22820
103. Zhang L, Meng Y, Dera P, Yang W, Mao WL, Mao HK. 2013. Single-crystal structure determination of (Mg,Fe)SiO_3 postperovskite. *PNAS* 110:6292–95
104. Bhattacharya A, Shen YF, Hefferan CM, Li SF, Lind J, et al. 2019. Three-dimensional observations of grain volume changes during annealing of polycrystalline Ni. *Acta Mater.* 167:40–50
105. Beaudoin A, Obstalecki M, Storer R, Tayon W, Mach J, et al. 2012. Validation of a crystal plasticity model using high energy diffraction microscopy. *Model. Simul. Mater. Sci. Eng.* 20:024006
106. Pagan D, Shade P, Barton N, Park JS, Kenesei P, et al. 2017. Modeling slip system strength evolution in Ti-7Al informed by in-situ grain stress measurements. *Acta Mater.* 128:406–17
107. Cereser A, Strobl M, Hall SA, Steuwer A, Kiyanagi R, et al. 2017. Time-of-flight three dimensional neutron diffraction in transmission mode for mapping crystal grain structures. *Sci. Rep.* 7:9561
108. Ludwig W, Schmidt S, Lauridsen E, Poulsen H. 2008. X-ray diffraction contrast tomography: a novel technique for three-dimensional grain mapping of polycrystals. I. Direct beam case. *J. Appl. Crystallogr.* 41:302–9
109. King A, Johnson G, Engelberg D, Ludwig W, Marrow J. 2008. Observations of intergranular stress corrosion cracking in a grain-mapped polycrystal. *Science* 321:382–85
110. King A, Herbig M, Ludwig W, Reischig P, Lauridsen E, et al. 2010. Non-destructive analysis of micro texture and grain boundary character from X-ray diffraction contrast tomography. *Nucl. Instrum. Methods B* 268:291–96
111. King A, Reischig P, Adrien J, Ludwig W. 2013. First laboratory X-ray diffraction contrast tomography for grain mapping of polycrystals. *J. Appl. Crystallogr.* 46:1734–40
112. McDonald SA, Reischig P, Holzner C, Lauridsen E, Withers P, et al. 2015. Non-destructive mapping of grain orientations in 3D by laboratory X-ray microscopy. *Sci. Rep.* 5:14665:1–11
113. Larson B, Yang W, Ice G, Budai J, Tischler J. 2002. Three-dimensional X-ray structural microscopy with submicrometre resolution. *Nature* 415:887–90

114. Barabash OM, Santella M, Barabash RI, Ice GE, Tischler J. 2010. Measuring depth-dependent dislocation densities and elastic strains in an indented Ni-based superalloy. *J. Miner.* 62:29–34
115. Shechtman Y, Eldar YC, Cohen O, Chapman HN, Miao J, Segev M. 2015. Phase retrieval with application to optical imaging. *IEEE Signal Proc. Mag.* 32:87–109
116. Robinson I, Vartanyants I, Williams G, Pfeifer M, Pitney J. 2001. Reconstruction of the shapes of gold nanocrystals using coherent X-ray diffraction. *Phys. Rev. Lett.* 87:195505
117. Ulvestad A, Singer A, Clark J, Cho H, Kim J, et al. 2015. Topological defect dynamics in operando battery nanoparticles. *Science* 348:1344–47
118. Yau A, Cha W, Kanan M, Stephenson G, Ulvestad A. 2017. Bragg coherent diffractive imaging of single-grain defect dynamics in polycrystalline films. *Science* 356:739–42
119. Phillips FHN, Das S, Karamched P, Hughes G, Douglas J, et al. 2019. Full, 3D-resolved lattice strain tensor measurements of specific crystallographic defects extracted from a bulk sample. arXiv:1903.04079 [cond-mat]
120. Maddali S, Allain M, Cha W, Harder R, Park JS, et al. 2019. Phase retrieval for Bragg coherent diffraction imaging at high X-ray energies. *Phys. Rev. A* 99:053838
121. Simons H, King A, Ludwig W, Detlefs C, Pantleon W, et al. 2015. Dark-field X-ray microscopy for multiscale structural characterization. *Nat. Commun.* 6:6098
122. Poulsen HF, Jakobsen A, Simons H, Ahl S, Cook P, Detlefs C. 2017. X-ray diffraction microscopy based on refractive optics. *J. Appl. Crystallogr.* 50:1441–56
123. Jakobsen AC, Simons H, Ludwig W, Yildirim C, Leemreize H, et al. 2019. Mapping of individual dislocations with dark-field X-ray microscopy. *J. Appl. Crystallogr.* 52:122–32
124. Lyckegaard A, Poulsen HF, Ludwig W, Fonda RW, Lauridsen EM. 2012. Box-scan: a novel 3DXRD method for studies of recrystallization and grain growth. *Mater. Sci. Forum* 715/716:518–20
125. Hayashi Y, Setoyama D, Hirose Y, Yoshida T, Kimura H. 2019. Intragranular three-dimensional stress tensor fields in plastically deformed polycrystals. *Science* 366:1492–96
126. Hayashi Y, Setoyama D, Seno Y. 2017. Scanning three-dimensional X-ray diffraction microscopy with a high-energy microbeam at SPring-8. *Mater. Sci. Forum* 905:157–64
127. Hayashi Y, Seno Y, Yoshida T. 2017. Orientation mapping of steel by scanning three-dimensional X-ray diffraction microscopy. *Acta Crystallogr. A* 70:C854
128. Laanait N, Zhang Z, Schlepütz CM. 2016. Imaging nanoscale lattice variations by machine learning of X-ray diffraction microscopy data. *Nanotechnology* 27:374002
129. Cherukara MJ, Nashed YSG, Harder RJ. 2018. Real-time coherent diffraction inversion using deep generative networks. *Sci. Rep.* 8:16520
130. Nygren KE, Pagan DC, Bernier JV, Miller MP. 2020. An algorithm for resolving intragranular orientation fields using coupled far-field and near-field high energy X-ray diffraction microscopy. *Mater. Charact.* 165:110366